LA-UR-97-577

Approved for public release; distribution is unlimited

Title: A Local Support-Operator Diffusion Discretization Scheme for Quadrilateral r-z Meshes

Author(s): Jim E. Morel
Randy M. Roberts
Mikhail J. Shashkov

Submitted to: Journal of Computational Physics

Los Alamos
National Laboratory

Los Alamos National Laboratory, an affirmative action/equal opportunity employer, is operated by the University of California for the U.S. Department of Energy under contract W-7405-ENG-36. By acceptance of this article, the publisher recognizes that the U.S. Government retains a nonexclusive, royalty-free license to publish or reproduce the published form of this contribution, or to allow others to do so, for U.S. Government purposes. Los Alamos National Laboratory requests that the publisher identify this article as work performed under the auspices of the U.S. Department of Energy. The Los Alamos National Laboratory strongly supports academic freedom and a researcher's right to publish; as an institution, however, the Laboratory does not endorse the viewpoint of a publication or guarantee its technical correctness.

Form 836 (10/96)

A Local Support-Operator Diffusion Discretization Scheme for Quadrilateral R-Z Meshes

J. E. Morel, Randy M. Roberts, and Mikhail J. Shashkov
University of California
Los Alamos National Laboratory
Los Alamos, NM 87545

Subject Classifications: 65N05, 65N20, 85A25, 82A70.

Running Head: Quadrilateral Differencing Scheme

Send proofs and page charges to:

Dr. J. E. Morel
Mail Stop B265
Los Alamos National Laboratory
Los Alamos, NM 87545

Abstract

We derive a cell-centered 2-D diffusion differencing scheme for arbitrary quadrilateral meshes in r-z geometry using a local support-operator method. Our method is said to be local because it yields a sparse matrix representation for the diffusion equation, whereas the traditional support-operator method yields a dense matrix representation. The diffusion discretization scheme that we have developed offers several advantages relative to existing schemes. Most importantly, it offers second-order accuracy even on meshes that are not smooth, rigorously treats material discontinuities, and has a symmetric positive-definite coefficient matrix. The only disadvantage of the method is that it has both cell-centered and cell-edge scalar unknowns as opposed to just cell-center scalar unknowns. Computational examples are given which demonstrate the accuracy and cost of the new scheme relative to existing schemes.

1 Introduction

The diffusion equation that we seek to solve can be expressed in the following general form:

$$\frac{\partial \phi}{\partial t} - \overrightarrow{\nabla} \cdot D \overrightarrow{\nabla} \phi = Q \quad , \tag{1}$$

where t denotes the time variable, ϕ denotes a scalar function that we refer to as the intensity, D denotes the diffusion coefficient, and Q denotes the source or driving function. It is sometimes useful to express Eq. (1) in terms of a vector function, $\overrightarrow{F}$, that we refer to as the flux:

$$\overrightarrow{F} = -D \overrightarrow{\nabla} \phi \quad . \tag{2}$$

We have taken the terms "intensity " and "flux" from the radiative transfer literature [1], but we have not explicitly considered the radiative diffusion equation because the subject of this paper relates to essentially any type of diffusion problem.

We define a cell-centered diffusion discretization scheme as one that numerically expresses the integral of Eq. (1) over each spatial cell. In particular, substituting from Eq. (2) into Eq. (1) and integrating that equation over a cell volume, we obtain:

$$\int_V \frac{\partial \phi}{\partial t} \, dV + \oint_{\partial V} \overrightarrow{F} \cdot \overrightarrow{n} \, dA = \int_V Q \, dV \quad , \tag{3}$$

where V denotes the cell volume, ∂V denotes the cell surface, and $\overrightarrow{n}$ denotes the outward-directed unit surface normal. Note that we used the divergence theorem to convert the

second integral in Eq. (3) from a volume integral to a surface integral. In physical terms, Eq. (3) generally represents a statement of particle or energy conservation over the cell. Thus we can simply state that cell-centered schemes (as we define them) are conservative over each mesh cell.

If one considers only non-orthogonal meshes with material discontinuities, existing vertex-centered diffusion discretizations are generally more advanced than cell-centered discretizations. This is primarily so because of the enormous success of Galerkin finite-element methods [2] and variants of those methods. Nonetheless, there are applications for for which cell-centered schemes appear to yield superior accuracy relative to vertex-centered schemes. For instance, when coupling diffusion calculations with cell-centered hydrodynamics calculations, a cell-centered diffusion scheme is highly desirable because it avoids the excessive numerical dissipation which can occur with vertex-centered diffusion schemes [3]. Our new scheme was developed with coupled radiation-diffusion/hydrodynamics applications in mind.

The following could be said of an ideal cell-centered diffusion scheme for 2-D quadrilateral meshes:

1. It gives second-order accuracy on both smooth and non-smooth meshes either with or without material discontinuities.

2. It has only cell-centered intensity unknowns.

3. It has a local stencil.

4. It has a symmetric positive-definite matrix representation for the diffusion equation, i.e., a positive-definite "diffusion matrix."

A local stencil is loosely defined to have coupling only between points that are spatially "close" in some sense. Cell-centered schemes such as those of Kershaw [4] and Pert [5], satisfy properties 2 through 4, but do not satisfy item 1. The scheme of Morel, Dendy, Hall, and White [6] satisfies properties 1 and 3, but does not satisfy properties 2 and 4. In particular, it has cell-edge intensity unknowns in addition to cell-center intensity unknowns, and it has an asymmetric diffusion matrix. The scheme of Van Beek, Van Nooyen, and Wesseling [7] satisfies properties 2 and 3, but not 1 and 4. In particular, it is non-convergent whenever the transverse component of the flux is discontinuous across a material interface. In addition, its diffusion matrix is asymmetric. The support-operator scheme of Shashkov and Steinberg [8] (derived only in x-y geometry) satisfies properties 1,2, and 4, but does not satisfy property 3. Their scheme has a dense diffusion matrix, which arises from a dense gradient matrix multiplied by a local divergence matrix. This difficulty can be circumvented for time-dependent calculations by transforming the dense equations into a local form in which the unknowns are the normal components of the flux located at cell faces. For

steady-state calculations, Shashkov and Steinberg recommend that the dense intensity-based system be solved using a conjugate-gradient approach. This would initially appear to require the multiplication of a vector and a dense matrix during each conjugate-gradient iteration. However, Shashkov and Steinberg show that this dense matrix-vector multiply can be effectively performed by solving a sparse diagonally-dominant SPD matrix system. This suggests a nested conjugate-gradient solution process: an outer conjugate gradient process solves the dense intensity-based system, and an inner conjugate-gradient process solves the sparse system associated with the dense matrix-vector multiply required for each outer conjugate-gradient iteration. Although this approach would probably be much more efficient than actually performing a dense matrix-vector multiply, it could nonetheless be quite expensive relative to simply solving a sparse SPD matrix representation for the diffusion equation.

The purpose of this paper is to use the support-operator approach [8] to derive a cell-centered diffusion discretization scheme for arbitrary quadrilateral meshes in r-z geometry. As previously indicated, the traditional cell-centered support-operator methodology used by Shashkov and Steinberg [8] leads to a dense diffusion matrix on non-orthogonal grids. Here we introduce a new variant of the cell-centered support-operator methodology which always leads to a local diffusion stencil at the expense of additional cell-edge intensity unknowns. Hence we refer to this new variant as a "local" support-operator method. We

stress that the local cell-center/cell-edge system that we obtain is equivalent to the dense cell-center system obtained with the traditional support-operator methodology in the sense that both systems yield the same the cell-centered intensity solution. Thus our new diffusion scheme represents a generalization to r-z geometry of the X-Y geometry scheme of Shashkov and Steinberg [8]. Interestingly, our new scheme is very similar to the scheme of Morel, Dendy, Hall, and White [6]. In particular these schemes have the same unknowns, the same cell-center stencil, and nearly the same cell-edge stencil (7-point for Morel, et.al., versus 9-point for the new scheme.) Of course, the significant difference between the schemes is that our new scheme has a symmetric positive-definite diffusion matrix whereas that of Morel, Dendy, Hall, and White [6] has an asymmetric diffusion matrix. The similarity between the schemes suggests that one could the construct a multigrid preconditioner for our scheme based upon the multigrid solution technique of Morel, Dendy, Hall, and White [6]. Indeed, we have developed such a preconditioner, and it is later shown that it performs quite well.

In summary, our new diffusion discretization scheme has the following properties:

- It gives second-order accuracy on both smooth and non-smooth meshes either with or without material discontinuities.

- It has both cell-centered and cell-edge intensity unknowns.

- It has a local stencil.

- It has a symmetric positive-definite matrix representation for the diffusion operator.

Note that it satisfies ideal properties 1, 3, and 4, but not 2. We know of no cell-centered scheme that satisfies all four ideal properties. We believe that our new scheme has the best combination of ideal properties of any previous scheme.

The remainder of this paper is organized as follows. We next explain the central theme of the support-operator method, describe our local methodology, and apply it to the simple case of a rectagular mesh in r-z geometry. This is followed by a derivation of our method for general quadrilateral meshes in r-z geometry. Our multigrid-preconditioned solution technique for logically-rectangular meshes is then described. Finally, computational results are given, followed by a summary and recommendations for future work.

2 The Support-Operator Method

In this section we describe the support-operator method. It is convenient at this point to define a modified gradient operator given by $-D\overrightarrow{\nabla}$. The diffusion operator of interest is given by the product of the divergence operator and the modified gradient operator: $-\overrightarrow{\nabla}\cdot D\overrightarrow{\nabla}$. The support-operator method is based upon the following three facts:

- Given appropriately defined scalar and vector inner products, the divergence and modified gradient operators are adjoint to one another.
- The adjoint of an operator varies with the definition of its associated inner products, but is unique for fixed inner products.
- The product of an operator and its adjoint is a self-adjoint positive-definite operator.

The mathematical details relating to these facts are given in Reference 8. Our support-operator method can be described in the simplest terms as follows:

1. Define discrete scalar and vector inner products that approximate the analytic inner products on a single arbitrary cell.
2. Define the discrete version of the divergence operator on a single arbitrary cell.
3. Use the adjoint property to define the discrete version of the modified gradient operator on a single arbitrary cell.
4. Obtain the global matrices by connecting adjacent mesh cells in such a way as to ensure that the adjoint relationship is maintained over the whole grid. This simply amounts to enforcing continuity of intensity and flux at the cell interfaces.
5. Combine the divergence matrix and the modified gradient matrix to obtain the diffusion matrix.

To make this process concrete, we generate the diffusion matrix for a rectangular mesh in r-z geometry. Our first step is to define the discrete unknowns. The global coordinate and mesh indexing is illustrated in Fig. 1. The local mesh indexing (local to each cell) is shown in Fig. 2. Each mesh cell is assumed to be homogeneous, but material properties may vary between cells. As shown in Fig. 3, the intensities (scalars) are defined to exist at both cell center: ($\phi^C_{i,j}$), and cell edge: ($\phi^R_{i,j}$, $\phi^B_{i,j}$, $\phi^L_{i,j}$, $\phi^T_{i,j}$). Note that the use of local indices implies that a quantity is uniquely associated with a single cell. Thus, for instance, one should not necessarily assume that $\phi^R_{i,j} = \phi^L_{i+1,j}$. As shown in Fig. 4, the vectors are defined in terms of surface-normal components located at the midpoints of the cell faces: ($f^R_{i,j}$, $f^B_{i,j}$, $f^L_{i,j}$, $f^T_{i,j}$,). For instance, $f^R_{i,j}$ denotes the dot product of $\overrightarrow{F}$ with the outward-directed unit surface normal located at the center of the right edge of cell i, j. The other surface-normal vector components are defined analogously. Since it takes two components to define a full vector, the full vectors are considered to be located at the cell corners: ($\overrightarrow{F}^{RB}_{i,j}$, $\overrightarrow{F}^{BL}_{i,j}$, $\overrightarrow{F}^{LT}_{i,j}$, $\overrightarrow{F}^{TR}_{i,j}$). As shown in Fig. 5, each corner vector has surface-components located on the two faces that share that corner, .e.g.,

$$\overrightarrow{F}^{RB}_{i,j} = \left(f^R_{i,j},\, f^B_{i,j}\right) \quad . \tag{4}$$

The other corner vectors are defined analogously.

As explained in Reference 8, the adjoint relationship between the modified gradient and divergence operators is embodied in the following integral identity:

$$\oint_{\partial V} \phi \overrightarrow{H} \cdot \overrightarrow{n} \, dA - \int_V D^{-1} \overrightarrow{H} \cdot D \overrightarrow{\nabla} \phi \, dV = \int_V \phi \overrightarrow{\nabla} \cdot \overrightarrow{H} \, dV \quad , \tag{5}$$

where ϕ is an arbitrary scalar function, $\overrightarrow{H}$ is an arbitrary vector function, V denotes a volume, ∂V denotes its surface, and $\overrightarrow{n}$ denotes the outward-directed unit normal associated with that surface. The vector $\overrightarrow{H}$ has the same mesh locations as the flux vector $\overrightarrow{F}$, but is not necessarily equal to $-D\overrightarrow{\nabla}\phi$. We stress that the function ϕ at this point represents an arbitrary scalar function, and not necesssarily the solution of the diffusion equation. The next step in our support-operator method is to discretize Eq. (5) over a single arbitrary cell in a special manner. Specifically, we explicitly discretize all but the modified gradient operator, which is expressed in an implicit form consistent with our choice of discrete unknowns. We assume indices of i, j for the arbitrary cell, but suppress these indices whenever possible in the discrete approximation to Eq. (5) that follows. We first discretize the surface integral:

$$\begin{aligned} \oint_{\partial V} \phi \overrightarrow{H} \cdot \overrightarrow{n} \, dA \;\; \approx \;\; & \phi^R h^R A^R + \phi^B h^B A^B + \\ & \phi^L h^L A^L + \phi^T h^T A^T \quad , \end{aligned} \tag{6}$$

where A^R denotes the face area associated with the right face of the cell:

$$A^R = 2\pi r_{i+\frac{1}{2}} \Delta z \quad , \tag{7}$$

(the remaining face areas are defined analogously) and where

$$\Delta z = z_{j+\frac{1}{2}} - z_{j-\frac{1}{2}} \quad . \tag{8}$$

Next we approximate the modified gradient volumetric integral:

$$\int_V - D^{-1} \overrightarrow{H} \cdot D \overrightarrow{\nabla} \phi \, dV \approx D^{-1} \left\{ \left(\overrightarrow{H}^{RB} \cdot \overrightarrow{F}^{RB} \right) V^{RB} + \left(\overrightarrow{H}^{BL} \cdot \overrightarrow{F}^{BL} \right) V^{BL} + \left(\overrightarrow{H}^{LT} \cdot \overrightarrow{F}^{LT} \right) V^{LT} + \left(\overrightarrow{H}^{TR} \cdot \overrightarrow{F}^{TR} \right) V^{TR} \right\} \quad , \tag{9}$$

where $\overrightarrow{F}$ denotes $-D \overrightarrow{\nabla} \phi$, and V^{RB} denotes the volumetric weight associated with the right-bottom corner:

$$V^{RB} = \frac{1}{4} \Delta r \Delta z \; 2\pi r_{i+\frac{1}{2}} \quad , \tag{10}$$

$$\Delta r = r_{i+\frac{1}{2}} - r_{i-\frac{1}{2}} \quad . \tag{11}$$

The volumetric weight associated with each corner consists of one-fourth the Cartesian cell volume multiplied by 2π times the value of the radius at that corner. These corner weights do not represent "true" volumes in any sense, but they do sum to the total cell volume:

$$V^{RB} + V^{BL} + V^{LT} + V^{TR} = V = \pi \left(r^2_{i+\frac{1}{2}} - r^2_{i-\frac{1}{2}} \right) \Delta z = 2\pi r_i \Delta r \Delta z \quad . \tag{12}$$

where

$$r_i = \frac{1}{2}\left(r_{i-\frac{1}{2}} + r_{i+\frac{1}{2}}\right) \qquad . \tag{13}$$

We choose these weights simply because they give us better properties than other more straightforward choices. The choice of weights is one of the many free parameters in the support-operator method. The remaining volumetric weights are defined in analogy with Eq. (10).

Finally, we approximate the divergence volumetric integral:

$$\int_V \phi \overrightarrow{\nabla} \cdot \overrightarrow{H} \; dV = \phi^C \left[h^R A^R + h^B A^B + h^L A^L + h^T A^T\right] \qquad . \tag{14}$$

Equations (6), (9), and (14) are certainly not unique, but they are fairly straightforward. For instance, Eq. (6) represents a face-centered second-order approximation to a surface integral. Equation (9) represents a corner-based volumetric integral consisting of a dot-product contribution from each pair of corner vectors. Equation (14) is a particularly simple second-order approximation which gives all of the weight to the cell-center value of ϕ while using a surface-integral formulation for $\overrightarrow{\nabla} \cdot \overrightarrow{H}$ that is analogous to the surface-integral used in Eq. (6).

Note that Eqs. (6), (9), and (14) define the discrete inner products discussed in Reference 8. Thus discretizing the fundamental integral identity expressed by Eq. (5) defines the discrete inner products associated with the adjoint relationship. We can now use this

relationship to solve for the modified gradient operator components by substituting from Eqs. (6), (9), and (14) into Eq. (5) and requiring that the resulting discretized identity hold for *all* discrete $\overrightarrow{H}$ and ϕ values. More specifically, we obtain an equation for the modified gradient component on a given face by setting the component of $\overrightarrow{H}$ on that face to unity while setting the components on all other faces to zero. For instance, setting $h^R = 1$, $h^B = 0$, $h^L = 0$, $h^T = 0$, we obtain an equation for f^R, which when solved yields:

$$f^R = -\frac{2D}{\Delta r}\left(\phi^R - \phi^C\right) \quad . \tag{15}$$

Equation (15) represents a standard expression for f^R that is exact when ϕ is lineary dependent upon r. Similar expressions are obtained for the other face components. Substituting these expressions into the discrete volume-integrated divergence operator that appears on the right side of Eq. (14) yields the discrete diffusion operator for a single cell:

$$\begin{aligned}\int_V -\overrightarrow{\nabla}\cdot D\,\overrightarrow{\nabla}\phi\, dV \approx \; & - \; \frac{2D}{\Delta r}\left[\left(\phi^R - \phi^C\right)A^R - \left(\phi^C - \phi^L\right)A^L\right] \\ & - \; \frac{2D}{\Delta z}\left[\left(\phi^T - \phi^C\right)A^T - \left(\phi^C - \phi^B\right)A^B\right] \quad .\end{aligned} \tag{16}$$

Combining expression (16) with standard point spatial discretizations for the time derivative and the source, we obtain the spatially-discrete diffusion equation:

$$\begin{aligned}& V\frac{\partial}{\partial t}\phi^C - \frac{2D}{\Delta r}\left[\left(\phi^R - \phi^C\right)A^R - \left(\phi^C - \phi^L\right)A^L\right] - \\ & \frac{2D}{\Delta z}\left[\left(\phi^T - \phi^C\right)A^T - \left(\phi^C - \phi^B\right)A^B\right] = Q^C V \quad ,\end{aligned} \tag{17}$$

Equation (17) represents the equation for cell centers. To obtain the equations for the cell-edge intensities, we "connect" the cells in such a way that our discrete version of Eq. (5) holds over the entire mesh. It is not difficult to see that this requirement will be met if the surface integral in Eq. (5) is made to cancel between cells, resulting in a surface integral over the outer mesh boundary. This can be achieved by making the surface-normal fluxes and the intensities continuous across cell interfaces. For instance, considering the right face of cell i, j, we require that:

$$\phi^R_{i,j} = \phi^L_{i+1,j} \quad , \tag{18}$$

and that

$$f^R_{i,j} = -f^L_{i+1,j} \quad . \tag{19}$$

Note that a "-" occurs within Eq. (19) because the surface normals associated with $f^R_{i,j}$ and $f^L_{i+1,j}$ are opposite in sign. Enforcing continuity of the intensities leaves us with one intensity unknown at each edge. Thus we can now uniquely refer to a cell-edge intensity in terms of its cell-edge index, i.e., the intensity at the right face of cell i, j and the left face of cell $i+1, j$ can now be uniquely referenced as $\phi_{i+\frac{1}{2},j}$. In addition, we can now neglect the superscript "C" for the cell-center intensities. The continuity-of-flux equation at each cell edge serves as the equation for the intensity at that edge. However, to maintain both

symmetry of the matrix and positive diagonal elements, we re-express Eq. (19) as follows:

$$-A_{i+\frac{1}{2},j} f^R_{i,j} - A_{i+\frac{1}{2},j} f^L_{i+1,j} = 0 \quad , \tag{20}$$

where

$$A_{i+\frac{1}{2},j} = A^R_{i,j} = A^L_{i+1,j} \quad . \tag{21}$$

Evaluating Eq. (20) in terms of the intensities, we obtain the equation for $\phi_{i+\frac{1}{2},j}$:

$$\frac{A_{i+\frac{1}{2},j} 2D_{i,j}}{\Delta z_i} \left(\phi_{i+\frac{1}{2},j} - \phi_{i,j}\right) - \frac{A_{i+\frac{1}{2},j} 2D_{i+1,j}}{\Delta z_{i+1}} \left(\phi_{i+1,j} - \phi_{i+\frac{1}{2},j}\right) = 0 \quad . \tag{22}$$

The continuity-of-flux equation at an interface on the outer boundary of the grid is analogous to Eq. (20). However, there is only one real cell adjacent to the interface rather than two. The normal flux component associated with cell 'outside' of the grid is given by an expression derived from the analytic boundary conditions. For instance, let us consider Eq. (20) evaluated at an interface on the right boundary of the mesh:

$$-A_{I+\frac{1}{2},j} f^R_{I,j} - A_{I+\frac{1}{2},j} f^L_{I+1,j} = 0 \quad , \tag{23}$$

where I denotes the maximum index of i. Cell $I+1, j$ does not exist, so we use the standard extrapolated boundary condition (standard in the radiation and neutron diffusion literature) to obtain an expression for $f^L_{I+1,j}$. This condition takes the following form at the boundary:

$$\phi + d_e \overrightarrow{\nabla} \phi \cdot \overrightarrow{n} = \phi_e \quad , \tag{24}$$

where d_e denotes the extrapolation distance, ϕ_e denotes the extrapolated intensity value, and $\overrightarrow{n}$ denotes the outward-directed unit normal vector. Note from Eq. (24) that this extrapolated condition is equivalent to a Robin or mixed condition. Recognizing that $D\overrightarrow{\nabla}\phi \cdot \overrightarrow{n}$ plays the role of $g^L_{I+1,j}$, we use Eq. (24) to obtain the desired expression:

$$f^L_{I+1,j} = \frac{D_{i,j}}{d_e}\left(\phi_e - \phi_{i+\frac{1}{2},j}\right) \quad . \tag{25}$$

Using Eqs. (15), (23), and (25), we obtain the equation for $\phi_{I+\frac{1}{2},j}$:

$$A_{I+\frac{1}{2},j}\left[\frac{2D_{I,j}}{\Delta z_I}\left(\phi_{I+\frac{1}{2},j} - \phi_{I,j}\right) - \frac{D_{I,j}}{d_e}\left(\phi_e - \phi_{I+\frac{1}{2},j}\right)\right] = 0 \quad . \tag{26}$$

A typical value for d_e is $2D$. This yields the Marshak boundary condition [1]. Note that if $d_e = 0$, one obtains the Dirichlet boundary condition with the boundary intensity given by ϕ_e. Furthermore, in the limit as $d_e \to \infty$, one obtains the Neumann condition.

Note from Eq. (22) that the continuity-of-flux equation for cell edges interior to the mesh relates the cell-edge intensity to the two adjacent cell-center intensities. Similarly note from Eq. (26) that the continuity-of-flux equation for cell edges on the outer boundary relates the cell-edge intensity to the only adjacent cell-center intensity and the extrapolated boundary intensity. Using these relationships to eliminate the edge intensities from Eq. (16) results in the standard 5-point cell-centered diffusion scheme. For instance, the following expression

is obtained for the normal flux on the right face of cell i, j:

$$f^R_{i,j} = -D_{i+\frac{1}{2},j} \frac{(\phi_{i+1,j} - \phi_{i,j})}{\Delta r_{i+\frac{1}{2}}} \quad , \tag{27}$$

where

$$-D_{i+\frac{1}{2},j} = \left\{ \left(\frac{\Delta r_i}{D_i} + \frac{\Delta r_{i+1}}{D_{i+1}} \right) \frac{1}{\Delta r_i + \Delta r_{i+1}} \right\}^{-1} \quad , \tag{28}$$

and

$$\Delta r_{i+\frac{1}{2}} = \frac{1}{2} \left(\Delta r_i + \Delta r_{i+1} \right) \quad . \tag{29}$$

Note that Eq. (27) contains only cell-center intensities. Further note that the definition for the cell-edge diffusion coefficient arises directly from the process of eliminating the cell-edge intensities. Thus we see that the method defines the cell-edge diffusion coefficient in terms of a specific averaging of the adjcent cell-center diffusion coefficients. In the case of a uniform mesh, this averaging reduces to the expected harmonic averaging. It is well known that the standard 5-point diffusion operator is symmetric positive-definite and has many desirable properties [9].

3 The New Scheme

In this section we derive our new quadrilateral diffusion discretization scheme. The procedure is analogous to that for the orthogonal-mesh case. Note that the r and z coordinates

carry full two-dimensional indices rather than the one-dimensional indices associated with an orthogonal mesh. A coordinate pair is assigned to each vertex in the mesh.

We again approximate Eq. (5) using a discrete approximation. For the case of a general quadrilateral, the general form of the discrete surface integral is identical to Eq. (6). However, the expressions for the face areas are slightly more complex than those of the orthogonal case. For instance:

$$A^R_{i,j} = 2\pi \left(\frac{r_{i+\frac{1}{2},j-\frac{1}{2}} + r_{i+\frac{1}{2},j+\frac{1}{2}}}{2} \right) \| \overrightarrow{r}_{i+\frac{1}{2},j+\frac{1}{2}} - \overrightarrow{r}_{i+\frac{1}{2},j-\frac{1}{2}} \| \quad , \tag{30}$$

where

$$\overrightarrow{r} = (r, z) \quad , \tag{31}$$

and where the symbol "$\| \cdot \|$" denotes the Euclidian vector norm. The other cell areas are defined in analogy with Eq. (30).

For the case of a general quadrilateral, the general form of the discrete modified gradient volumetric integral is identical to Eq. (9). However, there are two important differences in the definitions of certain quantities. First, since vectors are expressed in terms of normal surface components and the mesh is generally non-orthogonal, the dot product of two vectors cannot be taken in the standard way. In particular, in the orthogonal case, we can define the dot product in terms of the following inner product:

$$\overrightarrow{H}^{TR} \cdot \overrightarrow{F}^{TR} = \left\langle \overrightarrow{H}^{TR}, \overrightarrow{F}^{TR} \right\rangle = h^T f^T + h^R f^R \quad . \tag{32}$$

However, to take the dot product in the general non-orthogonal case, one must multiply either $\overrightarrow{H}$ or $\overrightarrow{F}$ by a particular SPD matrix, denoted by $\mathcal{S}$, before performing the inner product:

$$\begin{aligned} \overrightarrow{H}^{TR} \cdot \overrightarrow{F}^{TR} &= \left\langle \mathcal{S}^{TR}\overrightarrow{H}^{TR}, \overrightarrow{F}^{TR} \right\rangle = \left\langle \overrightarrow{H}^{TR}, \mathcal{S}^{TR}\overrightarrow{F}^{TR} \right\rangle \\ &= s^{TR}_{T,T} h^T f^T + s^{TR}_{T,R} h^T f^R + s^{TR}_{R,T} h^R f^T + s^{TR}_{R,R} h^R f^R \quad , \end{aligned} \tag{33}$$

where $s^{TR}_{T,R} = s^{TR}_{R,T}$. The $\mathcal{S}$ matrix is completely defined by the angle formed by the sides of the corner asssociated with the two vector components. This angle is depicted in Fig. 6 for the top-right corner. In particular,

$$\mathcal{S}^{TR} = \frac{1}{\sin^2(\Theta^{TR})} \begin{bmatrix} 1 & \cos(\Theta^{TR}) \\ \cos(\Theta^{TR}) & 1 \end{bmatrix} \quad . \tag{34}$$

Note that this matrix is invariant to the ordering of the surface-normal vector components. The $\mathcal{S}$ matrix is derived in Appendix A.

The second significant difference between the rectangular and quadrilateral cases arises in the volumetric weights assigned to each corner. In the orthogonal case, each corner weight is defined to be one-quarter of the cell area mutiplied by 2π times the radius at that cell corner. For the quadrilateral case, we define each corner weight as one-quarter of the area defined by the parallelogram associated with that corner multiplied by 2π times the radius at that corner. The parallelgram associated with the top-right corner is illustrated in

Fig. 7. The parallelograms associated with the other corners are analogously defined. Since these weights for the quadrilateral case do not necessarily sum to the total cell volume, we normalize them to ensure that they do so. For instance, the unnormalized volumetric weight for the top-right corner is given by

$$\tilde{V}^{TR} = \frac{1}{4}\left[\left(\overrightarrow{r}_{i-\frac{1}{2},j+\frac{1}{2}} - \overrightarrow{r}_{i+\frac{1}{2},j+\frac{1}{2}}\right)\cdot\left(\hat{r}_{i+\frac{1}{2},j-\frac{1}{2}} - \hat{r}_{i+\frac{1}{2},j+\frac{1}{2}}\right)\right] 2\pi r_{i+\frac{1}{2},j+\frac{1}{2}} \quad , \tag{35}$$

where $\hat{r}$ denotes a right-handed 90-degree rotation of the vector $\overrightarrow{r} = (r, z)$:

$$\hat{r} = (z, -r) \quad . \tag{36}$$

The remaining volumetric weights are defined in analogy with Eq. (35). The normalized volumetric weight for the top-right corner is given by

$$V^{TR} = \tilde{V}^{TR}\, V / \left(\tilde{V}^{TR} + \tilde{V}^{RB} + \tilde{V}^{BL} + \tilde{V}^{LT}\right) \quad , \tag{37}$$

where V denotes the true volume of cell i, j:

$$\begin{aligned} V = \quad & \left[\left(\overrightarrow{r}_{i-\frac{1}{2},j+\frac{1}{2}} - \overrightarrow{r}_{i+\frac{1}{2},j+\frac{1}{2}}\right)\cdot\left(\hat{r}_{i+\frac{1}{2},j-\frac{1}{2}} - \hat{r}_{i+\frac{1}{2},j+\frac{1}{2}}\right)\right] \\ & \frac{\pi}{3}\left(r_{i-\frac{1}{2},j+\frac{1}{2}} + r_{i+\frac{1}{2},j+\frac{1}{2}} + r_{i+\frac{1}{2},j-\frac{1}{2}}\right) + \\ & \left[\left(\hat{r}_{i-\frac{1}{2},j+\frac{1}{2}} - \hat{r}_{i-\frac{1}{2},j-\frac{1}{2}}\right)\cdot\left(\overrightarrow{r}_{i+\frac{1}{2},j-\frac{1}{2}} - \overrightarrow{r}_{i-\frac{1}{2},j-\frac{1}{2}}\right)\right] \\ & \frac{\pi}{3}\left(r_{i+\frac{1}{2},j-\frac{1}{2}} + r_{i-\frac{1}{2},j-\frac{1}{2}} + r_{i-\frac{1}{2},j+\frac{1}{2}}\right) \quad . \end{aligned} \tag{38}$$

Note that all of the corner weights are multiplied by the normalization factor appearing in Eq. (37).

It would seem that more straightforward corner weights could be chosen that would not require renormalization. However, we found the choice of corner weights critical to obtaining certain important properties. In particular, we found no other choice of weights that gave us both second-order accuracy on non-smooth meshes and spherically-symmetric solutions on spherically-symmetric $r - z$ meshes. See Appendix C for a demonstration of the spherically-symmetric properties of our scheme.

It is important to note that the expression given for the unnormalized corner weight in Eq. (35) gives a negative weight when the corner angle, Θ^{RT}, is greater than π. In this case, the cell is re-entrant and the corner volume is in fact negative. Negative weights can result in a diffusion matrix that is not positive-definite. To avoid this difficulty, we simply substitute the absolute value of the corner volume for the true corner volume in Eq. (35):

$$\tilde{V}^{TR} = \frac{1}{4}\left|\left(\overrightarrow{r}_{i-\frac{1}{2},j+\frac{1}{2}} - \overrightarrow{r}_{i+\frac{1}{2},j+\frac{1}{2}}\right)\cdot\left(\hat{r}_{i+\frac{1}{2},j-\frac{1}{2}} - \hat{r}_{i+\frac{1}{2},j+\frac{1}{2}}\right)\right| 2\pi r_{i+\frac{1}{2},j+\frac{1}{2}} \quad . \tag{39}$$

This procedure plays the role of the "parallelogram fixup" used in the MDHW scheme, but it is much simpler and just as effective.

For the case of a general quadrilateral, the general form of the discrete divergence volumetric integral is identical to that of Eq. (14). However, as previously noted for Eq. (6), the definition of the areas is given by Eq. (30) rather than Eq. (7).

To obtain expressions for the surface-normal components of the discrete gradient oper-

ator, we now proceed exactly as in the rectangular-mesh case. In particular, we substitute from Eqs. (6), (9), and (14) (using the quadrilateral-case definitions for the components of these equations) into Eq. (5), and then obtain an equation for the modified gradient component on a given face by setting the component of $\overrightarrow{H}$ on that face to unity while setting the components on all other faces to zero. In the orthogonal case, four independent linear equations for the modified gradient components were obtained. However, in the quadrilateral case, four coupled linear equations are obtained. It can be shown that this 4×4 system is non-singular as long as the quadrilateral is not degenerate, i.e., as long as it does not have coincident vertices or corner angles equal to 180 degrees. Nonetheless, solutions can be obtained for degenerate cases simply by taking appropriate limits. For instance, equations for triangles are easily obtained. A triangle is viewed as a quadrilateral with one face of zero area. The unknowns associated with such a degenerate face completely decouple from the other unknowns, allowing one to arbitrarily define the degenerate unknowns while leaving the other unknowns unaffected.

We solve the 4×4 system for the modified gradient components numerically rather than analytically, thus we cannot give explicit expressions for them. However, we can symbolically represent them in terms of the following 4×5 matrix (which we calculate

numerically):

$$\begin{bmatrix} f^R \\ f^B \\ f^L \\ f^T \end{bmatrix} = \begin{bmatrix} \mathcal{F}_{R,R} & \dots & \mathcal{F}_{R,C} \\ & & \\ & & \\ \mathcal{F}_{T,R} & \dots & \mathcal{F}_{T,C} \end{bmatrix} \begin{bmatrix} \phi^R \\ \phi^B \\ \phi^L \\ \phi^T \\ \phi^C \end{bmatrix} \quad , \tag{40}$$

In the general case, the matrix $\mathcal{F}$ is *full*.

The conditions for connecting cells are identical to those of the orthogonal case: continuity of intensity and flux across cell interfaces. Continuity of the intensity leads to a unique intensity at each cell edge. The equation for each cell-edge intensity expresses the continuity of flux. For the quadrilateral case, the flux-continuity equation has the same general form as Eq. (20), but the area elements are given by Eq. (30) rather than Eq. (7), and the modified gradient components are given by Eq. (40) rather than Eq. (15). Since the extrapolated boundary condition given in Eq. (24) is analytic, it can be applied to quadrilaterals as well as rectangles to obtain the normal flux component on a boundary face. For instance, Eq. (25) is valid on both rectangles and quadrilaterals. The point discretizations for the time derivative and source terms used in Eq. (17) are also used in the quadrilateral case. This completes the specification of our quadrilateral-mesh scheme.

As previously demonstrated, the cell-edge intensities on a rectangular mesh can be

eliminated via the continuity-of-flux equations to obtain a 5-point cell-centered diffusion scheme. Unfortunately, in the quadrilateral case this process yields a cell-centered diffusion scheme that has a full coefficient matrix. This is the *same* cell-centered scheme that one would obtain by applying the standard support-operator method of Shashkov and Steinberg [8] in conjunction with our definitions for the discrete inner products.

Our quadrilateral scheme yields a 5-point stencil for the cell-center equations and a 9-point stencil for the cell-edge equations. These stencils are illustrated in Figs. (8) and (9) respectively.

4 Solution of the Equations

We use a multigrid-preconditioned conjugate-gradient [10] method to solve our discrete diffusion equation. The preconditioner is based upon an approximate 5-point cell-center diffusion operator. As previously discussed, our cell-center/cell-edge system of equations can be reduced to a 5-point cell-center system when the mesh is orthogonal. This is possible because each cell-edge intensity becomes a function only of the two cell-centered intensities adjacent to it, and thus can be locally eliminated. This reduced edge/center coupling actually occurs whenever the corner S-matrices are diagonal, but they are diagonal only when the mesh is orthogonal. Taking this fact into account, we obtain our approximate cell-

center system simply by setting the off-diagonal elements of the corner S-matrices to zero, and then eliminating the cell-edge unknowns. In the preconditioning step, we do not fully solve this approximate system, but rather perform a set number of V-cycles using Dendy's black-box multigrid algorithm [11]. When the mesh is orthogonal, the "approximate" system is actually exact, but as the mesh becomes increasingly skewed, it becomes less accurate. Nonetheless, as shown in the next section, this method performs extremely well on moderately skewed meshes and fairly well on highly skewed meshes.

It is useful to consider certain details which arise when deriving and solving our approximate cell-center operator. Let us assume that our full cell-center/cell-edge equations are expressed in terms of the following matrix equation:

$$A\overrightarrow{\xi} = \overrightarrow{\eta} \quad , \tag{41}$$

where A is the coefficient matrx, $\overrightarrow{\xi}$ is the solution vector, and $\overrightarrow{\eta}$ is the source vector. The preconditioning step in the conjugate-gradient method consists of solving a matrix equation of the following form [10]:

$$\tilde{A}\overrightarrow{\delta\xi} = \overrightarrow{\delta\eta} \quad , \tag{42}$$

where $\tilde{A}$ denotes the approximation to A (called the preconditioner) and $\overrightarrow{\delta\eta}$ denotes a residual. The matrix appearing in Eq. (42) consists of the full cell-center/cell-edge system modified with the diagonal approximation for the corner $\mathcal{S}$-matrices. As can be seen from

Eq. (20), the cell-edge (continuity of flux) equations associated with our scheme normally do not contain sources. However, the cell-edge equations associated with Eq. (42) will have sources arising from the residual vector. Thus when the 5-point cell-center preconditioning system is derived from Eq. (42) by eliminating the cell-edge components of $\overrightarrow{\delta\xi}$, one must include the cell-edge residual components in the elimination process. Furthermore, after the V-cycles have been carried out to obtain the cell-center components of $\overrightarrow{\delta\xi}$, one must use these components together with the cell-edge equations to calculate the cell-edge components of $\overrightarrow{\delta\xi}$.

5 Computational Results

In this section we present computational results which demonstrate the accuracy of our method and the efficiency of our solution technique. The method of Morel, Dendy, Hall, and White [6] (MDHW) was computationally compared with several existing cell-centered Lagrangian-mesh diffusion differencing schemes in Reference 6. The accuracy of this method was clearly superior to that of the other schemes, but it was also significantly more expensive. Our method has the same unknowns as the MDHW scheme, the same cell-centered stencil, and nearly the same cell-edge stencil (our scheme has a 9-point edge stencil while the MDHW method has a 7-point edge stencil.) Nonetheless, our method

is less expensive than the MDHW scheme because we use conjugate-gradient iterations rather than fine-mesh line relaxations to solve our equations. The cost of solving the MDHW equations is dominated by the cost of performing such relaxations. We are able to use the conjugate-gradient solution technique because our coefficient matrix is SPD. The MDHW equations cannot be solved with the conjugate-gradient technique because the MDHW scheme has an asymmetric coefficient matrix.

We have performed many of the calculations that appear in Reference 6, but we have also performed several calculations relating to the convergence of our scheme on spherical meshes. The first set of calculations that we performed relate to the the accuracy of our scheme on highly skewed mesh. We consider the Kershaw-mesh problem given in Reference 6. A 10×10 Kershaw mesh is shown in Fig. 10. The following equation was solved:

$$-\frac{1}{r}\frac{\partial}{\partial r}\left[rD\frac{\partial \phi}{\partial r}\right] - \frac{\partial}{\partial z}\left[D\frac{\partial}{\partial z}\phi\right] = 0 \quad , \tag{43}$$

for $r \in [0,1]$, $z \in [0,1]$. The problem has reflective boundaries along $r = 0$ and $r = 1$, a Marshak vacuum boundary along $z = 1$ and a unit extrapolated Marshak boundary condition along $z = 0$. The solution to this problem is a linear function of z [6]. Although the MDHW scheme yields the exact solution to this problem, our scheme does not. We were unable to define inner product weights that would enable our method to yield exact

linear homogeneous solutions while maintaining all the other desirable properties of our scheme. Nonetheless, one would expect our scheme to converge to the exact solution as the mesh is refined. The intensity contours from our support-operator method are shown in Fig. 11. The exact contours are constant in r, but the support-operator contours are not constant. Rather they show some mesh distortion. However, the same calculation was repeated with a 48×48 mesh. This mesh is shown in Fig. 12. The corresponding intensity contours are shown in Fig. 13. The contours appear to be constant in r. This qualitatively demonstrates the convergence of our method on highly shewed meshes.

The second set of calculations addresses the accuracy of our method on highly distorted meshes with re-entrant cells. We solve the same problem defined above for the first set of calculations. A single calculation is performed on the 32×32 Shestakov mesh referred to in Reference 6. This mesh is shown in Fig. 14. It is clearly both highly skewed and highly distorted. It contains several cells that are re-entrant, and thus have negative corner volumes. In accordance with Eq. (39), we substitute the absolute value of a negative weight for the true weight, and then renormalize all four of the cell weights so that they sum to the correct volume. This is the analogue of the "parallelogram fixup" defined for the MDHW scheme. Our scheme, like the MDHW scheme, is non-convergent on meshes with re-entrant cells. This "fixup" procedure is simply intended to make the scheme more robust. The intensity contours are shown in Fig. 15. These contours are nearly constant in

r. This represents a very good result considering the fact that some of the mesh cells are re-entrant.

The third set of calculations addresses the convergence of our method on grids that are mildly distorted. Cylindrical random grids were used for similar purposes in Reference 6. We have used spherical random grids to demonstrate that our method converges on meshes containing triangles as well as quadrilaterals. These random grids were generated by moving each mesh vertex to a random position on a circle centered about the original vertex position. The radius of each circle was roughly one-fifth of the cell width. The 2-D $r - z$ equivalent of the following 1-D equation was solved:

$$-\frac{1}{R^2}\frac{\partial}{\partial R}\left[R^2 D \frac{\partial \phi}{\partial R}\right] = a + bR^2 \quad , \tag{44}$$

for $R \in [0, 1]$, where R denotes the spherical radius, i.e., $R = r^2 + z^2$, D denotes a region-dependent diffusion coefficient, and $a = b = 1$. The problem domain consists of a two region sphere illustrated in Fig. 16. The inner region is defined by $0 < R < 0.5$, and the outer region is defined by $0.5 < R < 1.0$. The diffusion coefficient is 1 in the inner region and 2 in the outer region. There are reflective boundary conditions along $z = 0$ and $r = 0$, and a Marshak vacuum boundary condition along $R = 1$. The analytic solution to this problem is:

$$\phi_1 = a\left(\frac{1}{3} + \frac{1}{24D_1} + \frac{1}{8D_2}\right) + b\left(\frac{2}{5} + \frac{1}{320D_1} + \frac{3}{64D_2}\right) - \frac{aR^2}{6D_1} - \frac{bR^4}{20D_1} \quad , \tag{45}$$

$$\phi_2 = a\left(\frac{1}{3}+\frac{1}{6D_2}\right)+b\left(\frac{2}{5}+\frac{1}{20D_2}\right)-\frac{aR^2}{6D_2}-\frac{bR^4}{20D_2} \quad , \tag{46}$$

where ϕ_1 and ϕ_2 respectively denote intensity solutions in the inner and outer regions, and D_1 and D_2 similarly denote the diffusion coefficients in the inner and outer regions.

Calculations were performed using our scheme on several randomly distorted grids. For instance , a 10×10 spherical random grid is shown in Fig. 17 and a 20×20 spherical random grid is shown in Fig. 18. The relative L_2 error norm is plotted in Fig. 19 for each calculation as a function of radial cell width. This relative norm consists of the standard L_2 norm of the cell-centered intensity errors divided by the L_2 norm of the cell-centered intensity solution. The error dependence expected with second-order convergence is also plotted in Fig. 19. The computed errors clearly agree with the expected errors, indicating that our scheme is second-order accurate on these randomly distorted spherical meshes that contain both a material discontinuity and triangular cells.

The fourth set of calculations is primarily intended to address the accuracy of our scheme relative to the MDHW scheme as a function of the mesh distortion. We performed calculations for a problem defined in Reference 6. The following equation was solved:

$$-\frac{\partial}{\partial z}\left[D\frac{\partial \phi}{\partial z}\right] = qz^2 \quad , \tag{47}$$

for $r \in [0,1]$, $z \in [0,1]$, where q is a constant. There are reflective boundary conditions along $r = 0$ and $r = 1$, and Marshak vacuum boundaries along $z = 0$ and $z = 1$. The

diffusion coefficient has a value of unity throughout the problem. The analytic solution to this problem is:

$$\phi = a + bz + cz^4 \quad , \tag{48}$$

where

$$a = \frac{q}{6}\left[\frac{1+8D}{1+4D}\right] \quad , \tag{49}$$

$$b = \frac{q}{12D}\left[\frac{1+8D}{1+4D}\right] \tag{50}$$

$$c = -\frac{q}{12D} \quad . \tag{51}$$

We have computed the solution to this problem using our support-operator scheme and the MDHW scheme on a 48×48 orthogonal mesh, a 48×48 random mesh, a 48×48 Kershaw mesh, and a 32×32 Sheshtakov mesh. The relative L_2 errors for these calculations are given in Table I. The support-operator and MDHW methods give the same error on the orthogonal mesh because they are identical on such meshes. They give comparable errors on all of the other meshes. This is similar to the results obtained by Steinberg and Shashkov when comparing their support-operator method with the MDHW method in $x-y$ geometry [8].

We also used the fourth set of calculations to compare the iterative convergence rate of our multigrid-preconditioned conjugate-gradient solution technique with the MDHW multigrid solution technique. The iterations required to converge the support-operator and

multigrid solution techniques are given in Table II. The solutions were considered converged when the L_2 norm of the residual vector divided by the L_2 norm of the source vector was less than 10^{-6}. It can be seen from Table II that mixed results were obtained. In two cases the support-operator scheme took fewer iterations and in two other cases the MDHW scheme took fewer iterations. Neither scheme ever took more than twice the iterations required by the other. Thus, the two schemes appear to be roughly comparable in terms of iterative convergence rate.

The support-operator and MDHW solution techniques significantly differ only in that the support-operator scheme uses a conjugate-gradient iteration in place of the line relaxations used in the MDHW scheme. The multigrid components of the two schemes are essentially identical. Because the support-operator and MDHW calculations had to be performed on different computers (a SUN workstation and a CRAY-YMP respectively,) a direct timing comparison between these two methods is difficult. Nonetheless, when one considers the particularly expensive nature of the line relaxations used in the MDHW scheme [6], it is clear that a conjugate-gradient iteration [10] must be significantly less costly. In support of this statement, we note that for the fourth set of calculations, only about one-third of the total solution time for our support-operator method was spent doing conjugate-gradient iterations, while over four-fifths of the total solution time of the MDHW scheme was spent doing line relaxations.

It is important to note from Table II that the iterative convergence rates for both our support-operator method and the MDHW method degrade as the mesh becomes increasingly distorted. This is not surprising since both methods use an approximate 5-point pure cell-centered diffusion operator to improve the iterative convergence rate, and these operators are highly inaccurate on distorted meshes relative to the fine-mesh schemes. Thus a more accurate preconditioner might significantly improve the performance of our solution technique on highly distorted meshes.

6 Summary and Future Work

We have developed a new "local" version of the support-operator method and applied it to the discretization of the diffusion operator on quadrilateral meshes. This local scheme yields a sparse banded diffusion matrix in contrast to the standard support-operator approach of Shashkov and Steinberg [8], which yields a dense diffusion matrix. However, the local approach requires edge intensity unknowns in addition to the cell-centered intensity unknowns, and thus is more costly than pure cell-centered schemes. However, our support-operator scheme yields a sparse banded symmetric positive-definite diffusion matrix, and converges with second-order accuracy even on grids that are not smooth and contain material discontinuities. We are unaware of any pure cell-centered scheme that has

these properties. In addition, our scheme conserves energy over each spatial cell, yields spherically-symmetric solutions on spherically-symmetric $r - z$ grids, and is sufficiently robust to provide a conservative solution even on meshes that contain re-entrant cells (e.g., boomerang and bowtie cells [6].) The only restriction on the re-entrant cells is that they must have a positive total volume. We believe that this extraordinary set of desirable properties makes our scheme a valuable alternative to traditional diffusion discretization schemes.

In the future we intend to investigate the solution of the system which results from eliminating the cell-centered intensity unknowns in our equations. This could significantly reduce the CPU time associated with our scheme. We also intend to investigate new approximate diffusion discretizations for preconditioning our support-operator equations. Our intent is to find a preconditioner that suffers less degradation as the mesh becomes increasingly distorted. An obvious candidate would be a 9-point pure cell-centered discretization. Finally, we intend to investigate the generalization of our quadrilateral-mesh method to 3-D hexahedral meshes.

Appendix A

In this appendix we derive the matrix S that is defined in Eq. (34). We begin by considering the top-right corner of the quadrilateral shown in Fig. 6. The flux vector associated with this corner is expressed in terms of its components with respect to the top-face and right-face normals:

$$\overrightarrow{F} = \left(\overrightarrow{F} \cdot \overrightarrow{n}^T, \overrightarrow{F} \cdot \overrightarrow{n}^R \right) = \left(f^T, f^R \right) \quad . \tag{52}$$

Note that the superscript "TR" for the vector $\overrightarrow{F}$ has been suppressed in Eq. (52) for simplicity. It is trivial to relate the standard r and z components of $\overrightarrow{F}$ to the normal components. In particular:

$$G\bar{F} = \overrightarrow{F} \quad , \tag{53}$$

where

$$G = \begin{bmatrix} n_r^T & n_z^T \\ n_r^R & n_z^R \end{bmatrix} \quad , \tag{54}$$

$$\bar{F} = \begin{bmatrix} f_r \\ f_z \end{bmatrix} \quad , \tag{55}$$

$$\overrightarrow{F} = \begin{bmatrix} f^T \\ f^R \end{bmatrix} \quad , \tag{56}$$

and where a subscript "r" denotes an r-component and a subscript "z" denotes a z-component. The vector $\bar{F}$ is said to be in the $r-z$ basis, while the vector $\overrightarrow{F}$ is said to be in the face-normal basis. Inverting G in Eq. (53), we get

$$\bar{F} = G^{-1}\overrightarrow{F} \quad . \tag{57}$$

By definition, the dot product of any two r-z basis vectors, $\bar{F}$ and $\bar{H}$, is given by

$$\bar{F} \cdot \bar{H} = f_r h_r + f_z h_z \quad . \tag{58}$$

It follows from Eqs. (57) and (58) that

$$\bar{F} \cdot \bar{H} = G^{-1}\overrightarrow{F} \cdot G^{-1}\overrightarrow{H} \quad , \tag{59}$$

where $\overrightarrow{H}$ is the face-normal counterpart of $\bar{H}$. Using the inner product defined in Eq. (32), we can re-express Eq. (59) as follows:

$$\begin{aligned} \bar{F} \cdot \bar{H} &= \left\langle \overrightarrow{F}, \left[G^{-1}\right]^t G^{-1} \right\rangle \overrightarrow{H} \\ &= \left\langle \left[G^{-1}\right]^t G^{-1}\overrightarrow{F}, \overrightarrow{H} \right\rangle \quad , \end{aligned} \tag{60}$$

where a superscript "t" denotes the matrix transpose. Comparing Eqs. (33) and (60), it is evident that

$$\mathcal{S}^{TR} = \left[G^{-1}\right]^t G^{-1} \quad . \tag{61}$$

Equation (34) can be obtained from Eqs. (54) and (61) after tedious but straightforward algebraic manipulations.

Appendix B

In this appendix we demonstrate that the coefficient matrix which arises from our discretization method is Symmetric Positive Definite (SPD). For simplicity, we ignore the contributions from the time-derivative term. If standard temporal differencing (e.g., fully-implicit or Crank-Nicholson) is used, this term will not affect the positive-definite character of the matrix because it contributes only to the diagonal elements.

Before we begin the demonstration we need to prove that the null space of a sum of matrices having Cholesky decompositions is the intersection of the null spaces of the individual matrices. Let $\mathcal{M}$ be such a sum, $\mathcal{M}_c$, each having a Cholesky decomposition,

$$\begin{aligned} \mathcal{M} &= \sum_c \mathcal{M}_c \quad , \\ &= \sum_c \mathcal{L}_c \mathcal{L}_c^t \quad , \end{aligned} \tag{62}$$

where $\mathcal{L}_c$ is a real lower triangular matrix with non-negative diagonals. The inner product of $\mathcal{M}$ with a vector x is then,

$$\begin{aligned} x^t \mathcal{M} x &= \sum_c x^t \mathcal{M}_c x \quad , \\ &= \sum_c x^t \mathcal{L}_c \mathcal{L}_c^t x \quad , \\ &= \sum_c y_c^t y_c \quad , \\ &\geq 0 \quad . \end{aligned} \tag{63}$$

The only way the equality can be satisfied is if each term in the sum is itself equal to zero, and therefore each y_c is the zero vector. This implies that x is in the null space of every $\mathcal{M}_c$ since,

$$\begin{aligned} \mathcal{M}_c x &= \mathcal{L}_c \mathcal{L}_c^t x \quad , \\ &= \mathcal{L}_c y_c \quad , \\ &= 0 \quad . \end{aligned} \tag{64}$$

In addition Eq. (63) demonstrates that $\mathcal{M}$ is Symmetric Positive Semidefinite (SPS). If the intersection of the null spaces are the empty set then the inequality in Eq. (63) becomes strictly greater, and $\mathcal{M}$ is SPD.

We begin the demonstration by considering the submatrix equation associated with a single quadrilateral:

$$\mathcal{M} \overrightarrow{\phi} = \overrightarrow{b} \, . \tag{65}$$

In this case $\mathcal{M}$ is a real 5×5 matrix operating on

$$\overrightarrow{\phi} = \begin{bmatrix} \phi^R \\ \phi^B \\ \phi^L \\ \phi^T \\ \phi^C \end{bmatrix} \in \mathcal{R}^{5\times 1}. \tag{66}$$

We first consider only the matrix equation for a single-cell mesh with reflective boundary conditions, and show that matrix for this system has a Cholesky decomposition. We then show that the matrix arising from a multi-cell mesh with reflective boundary conditions is also SPS, and determine the null space of this matrix. When the contributions from the vacuum boundaries are finally included, the resulting matrix will be shown to be SPD, by demonstrating that the vacuum boundary contributions reduce the null space of the matrix to the empty set.

There are several assumptions that must be made. The first is that the corner weights defined by Eq. (37) are positive. The second assumption is that all of the face areas defined by Eq. (30) are positive. All of these assumptions are valid if the quadrilaterals are non-degenerate. Our diffusion matrix is also SPD with certain types of degenerate cells, e.g., triangles, but we do not consider such cells here.

Consider the matrix formed by the weighted sum of the S-matrices defined in Eq. (34):

$$\mathcal{S} = V^{TR}\mathcal{S}^{TR} + V^{RB}\mathcal{S}^{RB} + V^{BL}\mathcal{S}^{BL} + V^{TL}\mathcal{S}^{LT} \quad . \tag{67}$$

Under the assumptions described above, $\mathcal{S}$ is a real 4×4 SPD matrix, as is its inverse, $\mathcal{S}^{-1}$. This matrix operates on the space of real 4-vectors representing the surface-normal components of vector quantities, e.g. (f^R, f^B, f^L, f^T).

We will define the matrix arising from the single-cell mesh, $\mathcal{M}$, in terms of two other

matrices,

$$\mathcal{A} = \begin{bmatrix} A^R \\ A^B \\ A^L \\ A^T \end{bmatrix} \in \mathcal{R}^{4\times 1} \quad , \tag{68}$$

and

$$\mathcal{W} = \begin{bmatrix} A^R & 0 & 0 & 0 \\ 0 & A^B & 0 & 0 \\ 0 & 0 & A^L & 0 \\ 0 & 0 & 0 & A^T \end{bmatrix} \in \mathcal{R}^{4\times 4} \quad . \tag{69}$$

Using these definitions, Eq. (40) becomes

$$\overrightarrow{F} = D\mathcal{S}^{-1}\left[-\mathcal{W}, \mathcal{A}\right] \overrightarrow{\phi} \quad . \tag{70}$$

The expression, $[-\mathcal{W}, \mathcal{A}]$, is a 4×5 real matrix.

The diffusion equation integrated over one cell is

$$\int_V \overrightarrow{\nabla} \cdot \overrightarrow{F}\, dV = Q \quad , \tag{71}$$

or equivalently,

$$\oint_{\partial V} \overrightarrow{F} \cdot \hat{n}\, dA = Q \quad . \tag{72}$$

In discrete form, this equation is

$$A^R f^R + \cdots + A^T f^T = Q \quad . \tag{73}$$

In block matrix form, the diffusion equation expressed in terms of ϕ becomes

$$D\mathcal{A}^t\mathcal{S}^{-1}\left[-\mathcal{W}, \mathcal{A}\right]\phi = Q \quad . \tag{74}$$

Reflective boundary conditions can be expressed in the following form for each face of the quadrilateral:

$$-A^R f^R = 0 \quad . \tag{75}$$

This equation can be written in block matrix form as

$$D\mathcal{W}\mathcal{S}^{-1}\left[\mathcal{W}, -\mathcal{A}\right]\overrightarrow{\phi} = \overrightarrow{0} \quad , \tag{76}$$

where $\overrightarrow{0}$ is a 4-vector.

Expressed together, Eqs. (76) and (74) represent five equations with five unknowns,

$$D\begin{bmatrix} \mathcal{W}\mathcal{S}^{-1}\mathcal{W} & -\mathcal{W}\mathcal{S}^{-1}\mathcal{A} \\ -\mathcal{A}^t\mathcal{S}^{-1}\mathcal{W} & \mathcal{A}^t\mathcal{S}^{-1}\mathcal{A} \end{bmatrix}\overrightarrow{\phi} = \begin{bmatrix} \overrightarrow{0} \\ Q \end{bmatrix} \quad . \tag{77}$$

This is the form for the matrix $\mathcal{M}$ defined in Eq. (65). We will now show that this matrix has a Cholesky decomposition and determine its null space.

To demonstrate the matrix from Eq. (77),

$$\mathcal{M} = D \begin{bmatrix} \mathcal{W}\mathcal{S}^{-1}\mathcal{W} & -\mathcal{W}\mathcal{S}^{-1}\mathcal{A} \\ -\mathcal{A}^t\mathcal{S}^{-1}\mathcal{W} & \mathcal{A}^t\mathcal{S}^{-1}\mathcal{A} \end{bmatrix} \quad , \tag{78}$$

has a Cholesky decomposition, we rely on the fact that any SPD matrix may be written as a product of a lower-triangular matrix with positive diagonals and its transpose [12]. The matrix $\mathcal{S}^{-1}$ is SPD and can be expressed as,

$$\mathcal{S}^{-1} = \mathcal{L}_{\mathcal{S}}{\mathcal{L}_{\mathcal{S}}}^t \quad , \tag{79}$$

with $\mathcal{L}_{\mathcal{S}}$ having positive diagonal elements.

This matrix, $\mathcal{M}$ can be shown to be the product of the following lower-triangular matrix,

$$\mathcal{L}_{\mathcal{M}} = \begin{bmatrix} \mathcal{W}\mathcal{L}_{\mathcal{S}} & \overrightarrow{0} \\ -\mathcal{A}^t\mathcal{L}_{\mathcal{S}} & 0 \end{bmatrix} \quad , \tag{80}$$

and its transpose. Since $\mathcal{W}$ is a positive diagonal matrix, the product $\mathcal{W}\mathcal{L}_{\mathcal{S}}$ is lower-triangular with positive diagonals; therefore, $\mathcal{L}_{\mathcal{M}}$ is lower-triangular with 4 positive diagonals and 1 zero diagonal. This demonstrates that $\mathcal{M}$ has a Cholesky decomposition.

We will now show that the null space of $\mathcal{M}$ has dimension 1 by finding all solutions $(\overrightarrow{b}, \nu)$ to the equation

$$\mathcal{M} \begin{bmatrix} \overrightarrow{b} \\ \nu \end{bmatrix} = \begin{bmatrix} \overrightarrow{0} \\ 0 \end{bmatrix} \quad . \tag{81}$$

These solutions form the null space of $\mathcal{M}$,

$$\begin{aligned} \text{null}(\mathcal{M}) &= \text{span}\left\{ \begin{bmatrix} \mathcal{W}^{-1}\mathcal{A} \\ 1 \end{bmatrix} \right\} \quad , \qquad (82) \\ &= \text{span}\left\{ \begin{bmatrix} 1 \\ \vdots \\ 1 \end{bmatrix} \right\} \in \mathcal{R}^{5\times 1} \quad . \qquad (83) \end{aligned}$$

To determine that the matrix resulting from a multi-cell mesh with reflective boundary conditions is SPS, we will extend matrix $\mathcal{M}$ from one cell to the full N-dimensional solution space by adding zero entries on the rows and columns representing unknowns not contained in the cell. We will label this matrix by the cell index, c,

$$\mathcal{M} \in \mathcal{R}^{5\times 5} \longrightarrow \mathcal{M}_c \in \mathcal{R}^{N\times N} \quad . \qquad (84)$$

We define $\mathbf{B}_c$ as the set of the indices for the unknowns contained by the c'th cell,

$$\mathbf{B}_c \equiv \{\ i\ :\ (\mathcal{M}_c)_{i,j} \neq 0 \quad \text{for some } j\ \} \quad . \qquad (85)$$

The null space of $\mathcal{M}_c$ contains any vector with the same value at the columns indicated by $\mathbf{B}_c$,

$$\text{null}(\mathcal{M}_c) = \text{span}\left\{\ [a_1, a_2, \ldots, a_N]^t\ :\ a_i = 1 \text{ for } i \in \mathbf{B}_c\ \right\} \quad . \qquad (86)$$

In order to assemble the single-cell matrices, $\mathcal{M}_c$, into the total N $\times$ N matrix, $\mathcal{M}$, we impose current continuity conditions between adjoining interior faces. Consider two cells,

the right side of the first cell adjoining the left side of the second cell. Separately each cells' matrix equations for this face are

$$-A_1^R f_1^R = 0 \quad , \tag{87}$$

$$-A_2^L f_2^L = 0 \quad . \tag{88}$$

When these equations are added together, noting that the shared face areas are identical, $A_1^R = A_2^L$, we arrive at the current continuity condition,

$$-A_1^R f_1^R - A_2^L f_2^L = 0 \quad , \tag{89}$$

$$f_1^R + f_2^L = 0 \quad . \tag{90}$$

Therefore, the entire matrix is the sum of the single-cell matrices,

$$\mathcal{M} = \sum_c \mathcal{M}_c \quad . \tag{91}$$

This matrix is SPS, since the sum of matrices with Cholesky decompositions is guaranteed to be SPS.

The null space of a sum of matrices with Cholesky decompositions is the intersection of the cell matrix null spaces,

$$\text{null}(\mathcal{M}) = \bigcap_c \text{null}(\mathcal{M}_c) \quad . \tag{92}$$

Since the union of all of the $\mathbf{B}_c$ is the set from 1 to N,

$$\bigcup_c \mathbf{B}_c = \{1, 2, \ldots, N\} \quad , \tag{93}$$

the null space of $\mathcal{M}$ contains all vectors with the same value in all of its columns,

$$\text{null}(\mathcal{M}) = \text{span}\left\{ \begin{bmatrix} 1 \\ \vdots \\ 1 \end{bmatrix} \right\} \in \mathcal{R}^{N \times 1} \quad . \tag{94}$$

Now consider that there is at least one cell, v, that contains a vacuum boundary face, and without loss of generality we will assume that this face is the rightmost face. The vacuum boundary conditions for this cell can be expressed in the following form,

$$A_v^R \left(\lambda_v^R \phi_v^R - f_v^R \right) = 0 \quad . \tag{95}$$

Although it might not be obvious, this form is equivalent to that expressed in Eq. (24). For instance, the Marshak boundary condition is obtained if $\lambda_v^R = 1/2$.

This cell will contribute an additional term to the sum in Eq. (91),

$$\mathcal{M} = \sum_c \mathcal{M}_c + \mathcal{M}'_v \quad . \tag{96}$$

This extra matrix contains a $A_v^R \lambda_v^R$ term on the diagonal for the unknown on the vacuum

face, i.e.

$$\mathcal{M}'_v = \begin{bmatrix} 0 & 0 & 0 \\ 0 & A_v^R \lambda_v^R & 0 \\ 0 & 0 & 0 \end{bmatrix} \in \mathcal{R}^{N \times N} \quad . \tag{97}$$

The matrix, $\mathcal{M}'_v$, with all zeros except for one positive value on the vacuum face unknown diagonal, obviously has a Cholesky decomposition. It's null space contains all vectors with a zero on the vacuum face column. It is obvious that this null space is disjoint from the intersection of the null spaces of the matrices forming the sum in Eq. (91), and therefore

$$\begin{aligned} \text{null}(\mathcal{M}) &= \bigcap_c \text{null}(\mathcal{M}_c) \bigcap \text{null}(\mathcal{M}'_v) \quad , & (98) \\ &= \emptyset \quad , & (99) \end{aligned}$$

the empty set. Using the proof from earlier in the appendix we have demonstrated that $\mathcal{M}$ is SPD.

Appendix C

In this appendix we demonstrate that our new solution method preserves the spherical symmetry of a solution on a spherically symmetric mesh. A spherically-symmetric r-z mesh is illustrated in Fig. 10. The mesh coordinates are labeled with the i axis in the $\hat{\theta}$

direction and the j axis in the $\hat{R}$ direction, with

$$R = \sqrt{r^2 + z^2} \quad . \tag{100}$$

In order to demonstrate that this scheme perserves a spherically symmetric solution we will show that the new scheme admits a solution with cell-centered intensities independent of the i coordinate, i.e.,

$$\phi^C_{i,j} = \phi^C_j \quad , \tag{101}$$

and that these symmetric intensities lead to fluxes, $f_{i,j}$, independent of i, having only radial components, i.e.

$$\begin{aligned} f^B_{i,j} &= f^B_j \quad , \\ f^T_{i,j} &= f^T_j \quad , \\ f^R_{i,j} &= 0 \quad , \\ f^L_{i,j} &= 0. \end{aligned} \tag{102}$$

To establish the above relations we must first show that the factor used to scale the volumetric weights in Eq. (37) is independent of i,

$$W_{i,j} = \frac{V_{i,j}}{\tilde{V}^{TR}_{i,j} + \tilde{V}^{RB}_{i,j} + \tilde{V}^{BL}_{i,j} + \tilde{V}^{LT}_{i,j}} \quad , \tag{103}$$

$$= W_j \quad . \tag{104}$$

The unnormalized volumetric weights for the corners are related to the parallelepiped volumes, $\mathcal{V}$, by

$$\tilde{V}_{i,j}^{TR} = 2\pi r_{i+\frac{1}{2},j+\frac{1}{2}} \mathcal{V}_{i,j}^{TR} \quad , \tag{105}$$

$$\tilde{V}_{i,j}^{RB} = 2\pi r_{i+\frac{1}{2},j-\frac{1}{2}} \mathcal{V}_{i,j}^{RB} \quad , \tag{106}$$

$$\tilde{V}_{i,j}^{BL} = 2\pi r_{i-\frac{1}{2},j-\frac{1}{2}} \mathcal{V}_{i,j}^{BL} \quad , \tag{107}$$

$$\tilde{V}_{i,j}^{LT} = 2\pi r_{i-\frac{1}{2},j+\frac{1}{2}} \mathcal{V}_{i,j}^{LT} \quad . \tag{108}$$

Due to the regularity of this mesh the parallelpiped volumes are simply related,

$$\mathcal{V}_{i,j}^{TR} = \mathcal{V}_{i,j}^{LT} = \mathcal{V}_{j+\frac{1}{2}} \quad , \tag{109}$$

$$\mathcal{V}_{i,j}^{RB} = \mathcal{V}_{i,j}^{BL} = \mathcal{V}_{j-\frac{1}{2}} \quad , \tag{110}$$

where

$$\mathcal{V}_{j-\frac{1}{2}} = \frac{R_{j-\frac{1}{2}}}{R_{j+\frac{1}{2}}} \mathcal{V}_{j+\frac{1}{2}} \quad , \tag{111}$$

and the expression for the volumetric weight scaling factor Eq. (103) is,

$$W_j = \frac{1}{6} \frac{R_{j-\frac{1}{2}}^2 + R_{j-\frac{1}{2}} R_{j+\frac{1}{2}} + R_{j+\frac{1}{2}}^2}{R_{j-\frac{1}{2}}^2 + R_{j+\frac{1}{2}}^2} \quad , \tag{112}$$

where Eq. (40) was substituted for $V_{i,j}$.

There are two sets of equations that we will examine. The first set is used to find an expression for $f_{i,j}^T$ from cell i, j and its top neighbor, cell $i, j+1$. This expression will be

found to be independent of i for a spherically-symmetric problem. The second set is used to find an expression for $f^R_{i,j}$ from cell i,j and its right neighbor, cell $(i+1,j)$. This expression will be found to be zero for a spherically-symmetric problem. Due to current continuity we will not need to examine $f^B_{i,j}$, nor $f^L_{i,j}$. These expressions will be derived referring to Fig. 20.

To derive an expression for $f^T_{i,j}$ we use the ϕ^T equation for cell i,j and the ϕ^B equation for cell $i,j+1$:

$$\frac{V^{LT}_{i,j}}{\sin^2\alpha}\left(f^T_{i,j}+\cos\alpha\, f^L_{i,j}\right)+\frac{V^{TR}_{i,j}}{\sin^2\alpha}\left(f^T_{i,j}+\cos\alpha\, f^R_{i,j}\right)=-DA^T_{i,j}\left(\phi^T_{i,j}-\phi^C_{i,j}\right) \tag{113}$$

$$\frac{V^{BL}_{i,j+1}}{\sin^2\gamma}\left(f^B_{i,j+1}+\cos\gamma\, f^L_{i,j+1}\right)+\frac{V^{RB}_{i,j+1}}{\sin^2\gamma}\left(f^B_{i,j+1}+\cos\gamma\, f^R_{i,j+1}\right) = -DA^B_{i,j+1}\left(\phi^B_{i,j+1}-\phi^C_{i,j+1}\right). \tag{114}$$

The $\sin^2\alpha$ and $\sin^2\gamma$ terms arise from the form of the $\mathcal{S}^{-1}$ matrix.

We now rely on the continuity between neighbor cells, i.e.

$$\phi^B_{i,j+1} = \phi^T_{i,j} \quad , \tag{115}$$

$$f^B_{i,j+1} = -f^T_{i,j} \quad , \tag{116}$$

and geometric relations between the two cells,

$$\sin\gamma = \sin\alpha \quad \text{, independent of } i, \tag{117}$$

to eliminate the cell-edge unknown, $\phi^T_{i,j}$, from the equations. In doing so we assume that the intensities and volume scaling factors depend only on j, and that $f^L = f^R = 0$:

$$\frac{W_j + W_{j+1}}{\sin^2\alpha}\mathcal{V}_{j+\frac{1}{2}} f^T_{i,j} = -\frac{1}{2}D\|\Delta\overrightarrow{r}_{j+\frac{1}{2}}\|\left(\phi^C_{j+1} - \phi^C_j\right) \quad , \tag{118}$$

with

$$\|\Delta\overrightarrow{r}_{j+\frac{1}{2}}\| = \|\overrightarrow{r}_{i+\frac{1}{2},j+\frac{1}{2}} - \overrightarrow{r}_{i-\frac{1}{2},j+\frac{1}{2}}\| \quad \text{, independent of } i. \tag{119}$$

We have used Eqs. (21), (30), (104), (105)–(108), and (109) to arrive at Eq. (118). It is clear that $f^T_{i,j}$ depends only on j:

$$f^T_{i,j} = f^T_j. \tag{120}$$

Now that we have shown that the first set of equations, with the assumption of radial fluxes, yields spherically-symmetric fluxes, we will demonstrate that spherically-symmetric fluxes yield radial fluxes for the second set of equations.

To derive an expression for $f^R_{i,j}$ we use the ϕ^R equation for cell i,j and the ϕ^L equation for cell $i+1,j$, respectively:

$$\frac{V^{TR}_{i,j}}{\sin^2\alpha}\left(f^R_{i,j} + \cos\alpha\, f^T_{i,j}\right) + \frac{V^{RB}_{i,j}}{\sin^2\beta}\left(f^R_{i,j} + \cos\beta\, f^B_{i,j}\right) = -DA^R_{i,j}\left(\phi^R_{i,j} - \phi^C_{i,j}\right) \quad , \tag{121}$$

$$\frac{V^{LT}_{i+1,j}}{\sin^2\alpha}\left(f^L_{i+1,j} + \cos\alpha\, f^T_{i+1,j}\right) + \frac{V^{BL}_{i+1,j}}{\sin^2\beta}\left(f^L_{i+1,j} + \cos\beta\, f^B_{i+1,j}\right) = -DA^L_{i+1,j}\left(\phi^L_{i+1,j} - \phi^C_{i+1,j}\right) \quad . \tag{122}$$

We now rely on the continuity between neighbor cells, i.e.

$$\phi^L_{i+1,j} = \phi^R_{i,j} \quad , \tag{123}$$

$$f^L_{i+1,j} = -f^R_{i,j} \quad , \tag{124}$$

and geometric relations between the two cells,

$$\sin\beta = \sin\alpha \quad \text{, independent of } i, \tag{125}$$

$$V^{LT}_{i+1,j} = V^{TR}_{i,j} \quad , \tag{126}$$

$$V^{BL}_{i+1,j} = V^{RB}_{i,j} \quad , \tag{127}$$

to eliminate $f^L_{i+1,j}$ and the cell-edge unknowns, ϕ^R_{ij} and $\phi^L_{i+1\,j}$, from equations (121) and (122). In doing so we will assume that the intensities, $\phi^C_{i,j}$, volume scaling factors, $W_{i,j}$, and radial fluxes, $f^T_{i,j}$ and $f^B_{i,j}$, depend only on j (independent of i). Equations (121) and (122) become,

$$\frac{2}{\sin^2\alpha}\left[V^{TR}_{i,j} + V^{RB}_{i,j}\right] f^R_{i,j} = -DA^R_{i,j}\left(\phi^C_{i+1,j} - \phi^C_{i,j}\right) \quad , \tag{128}$$

$$= -DA^R_{i,j}\left(\phi^C_j - \phi^C_j\right) \quad , \tag{129}$$

$$= 0 \quad . \tag{130}$$

Since factor in front of $f^R_{i,j}$ is non-zero, we must conclude that

$$f^R_{i,j} = 0 \quad , \tag{131}$$

which implies that a spherically symmetric initial solution results in a radial flux.

We have succeeded in demonstrating that the new method, on a regular spherical r-z mesh, preserves a spherical solution that consists of fluxes with only radial components.

Acknowledgment

This work was performed under the auspices of the U.S. Department of Energy.

References

[1] G. C. Pomraning, *Equations of Radiation Hydrodynamics*, Volume 54 of the International Series of Monographs in Natural Philosophy, Edited by D. ter Haar, Pergamon Press, New York, (1973).

[2] O. C. Zienkiewicz, *The Finite Element Method*, McGraw-Hill, London, 3rd Edition (1977).

[3] A. I. Shestakov, J. A. Harte, and D. S. Kershaw,"Solution of the Diffusion Equation by Finite Elements in Lagrangian Hydrodynamics Codes," *J. Comp. Phys.*, **76**, 385 (1988).

[4] D. S. Kershaw, "Differencing of the Diffusion Equation in Lagrangian Hydrodynamic Codes," *J. Comp. Phys.*, **39**, 375 (1981).

[5] G. J. Pert, "Physical Constraints in Numerical Calculations of Diffusion," *J. Comp. Phys.*, **42**, 20 (1981).

[6] J. E. Morel, J. E. Dendy, Jr., Michael Hall, and Stephen White, "A Cell-Centered Lagrangian-Mesh Diffusion Differencing Scheme," *J. Comp. Phys.*, **103**, 286 (1992).

[7] P. Van Beek, R. R. P. Van Nooyen, and P. Wesseling, "Accurate Discretization of Gradients on Non-Uniform Staggered Grids," *J. Comp. Phys.*, **117**, 364 (1995).

[8] M. J. Shashkov and S. Steinberg, "Solving Diffusion Equations with Rough Coefficients in Rough Grids," *Journal of Computational Physics*, **129**, 383 (1996).

[9] A. Weiser and M. F. Wheeler, "On Convergence of Block-Centered Finite Differences for Elliptic Problems," *SIAM J. Numer. Anal.*, **25**, 351 (1988).

[10] Gene H. Golub and Charles F. Van Loan, *Matrix Computations*, The Johns Hopkins University Press, Baltimore, (1983).

[11] J. E. Dendy, Jr., "Black Box Multigrid," *J. Comp. Phys.* **48**, 366 (1982).

[12] J. Stoer and R. Bulirsch, *Introduction to Numerical Analysis*, Springer-Verlag, New York, (1980).

Table I: Comparison of Support-Operator and MDHW Accuracy.

Mesh	SO Error	MDHW Error
48×48 orthogonal	4.72×10^{-5}	4.72×10^{-5}
48×48 random	4.31×10^{-5}	4.38×10^{-5}
48×48 Kershaw	2.23×10^{-4}	2.19×10^{-4}
32×32 Shestakov	6.78×10^{-4}	7.50×10^{-4}

Table II: Iterative Convergence Comparison of Support-Operator and MDHW Schemes.

Mesh	SO Iterations	MDHW Iterations
48×48 orthogonal	3	6
48×48 random	11	8
48×48 Kershaw	59	84
32×32 Shestakov	94	50

Figure Captions

1. Global Coordinate and Mesh Indexing. The global indexing for mesh cell i, j is illustrated. Vertices are marked by circles and carry half-integer indices. Face centers are marked by squares and carry both integer and half-integer indices. Cell centers are marked by a triangle and carry integer indices. The fundamental mesh coordinates lie at the vertices. If the mesh is orthogonal, the r-coordinates need carry only the index i and the z-coordinates need carry only the index j, but if the mesh is non-orthogonal, both indices are required for each coordinate pair.

2. Local Mesh Indexing. Corners are denoted by TR (Top-Right), RB (Right-Bottom), BL (Bottom-Left), and LT (Left-Top). Faces are denoted by R (Right), B (Bottom), L (Left), and T (Top). Note that local indexing can accomodates multiple unknowns at the same location. For instance, the intensity on the right face of cell i, j need not necessarily be equal to the intensity on the left face of cell $i + 1, j$.

3. Locations of Intensity Unknowns. The intensity unknowns are located at cell centers and face centers.

4. Locations of Vector Component Unknowns. One vector component is located at each face center and represents the dot product of the flux vector with the outward-directed face normal vector.

5. Effective Locations of Complete Flux Vectors. Full flux vectors are considered to be located at cell corners and are composed of the components on the two faces associated with each corner. This is illustrated for the top-right corner vector, which is composed of the top-face and right face flux components.

6. S-Matrix Angle. The angle appearing in the S-matrix for the top-right corner is illustrated.

7. Corner Parallelogram. The parallelogram associated with the top-right corner of a quadrilateral overlays that quadrilateral.

8. Cell-Center Stencil. The lightly-colored circle marks the location of the cell-center intensity to which this equation corresponds.

9. Cell-Edge Stencil. The lightly-colored circle marks the location of the cell-edge intensity to which this equation corresponds.

10. 10×10 Kershaw Mesh.

11. Intensity Contours for 10×10 Kershaw Mesh. The exact contours are constant in r.

12. 48×48 Kershaw Mesh.

13. Intensity Contours for 48×48 Kershaw Mesh. The exact contours are constant in r.

14. 32×32 Shestakov Mesh.

15. Intensity Contours for 32×32 Shestakov Mesh. The exact contours are constant in r.

16. Spherical Test Problem Domain.

17. 10×10 Random Spherical Mesh. Note that the interface between material regions is not distorted.

18. 20×20 Random Spherical Mesh. Note that the interface between material regions is not distorted.

19. Error Versus Radial Cell Width.

20. Spherically-Symmetric Mesh.

Figure 1: JCP: Morel, Roberts, and Shashkov, "A Local Support-Operator Diffusion Discretization Scheme for Quadrilateral r-z Meshes."

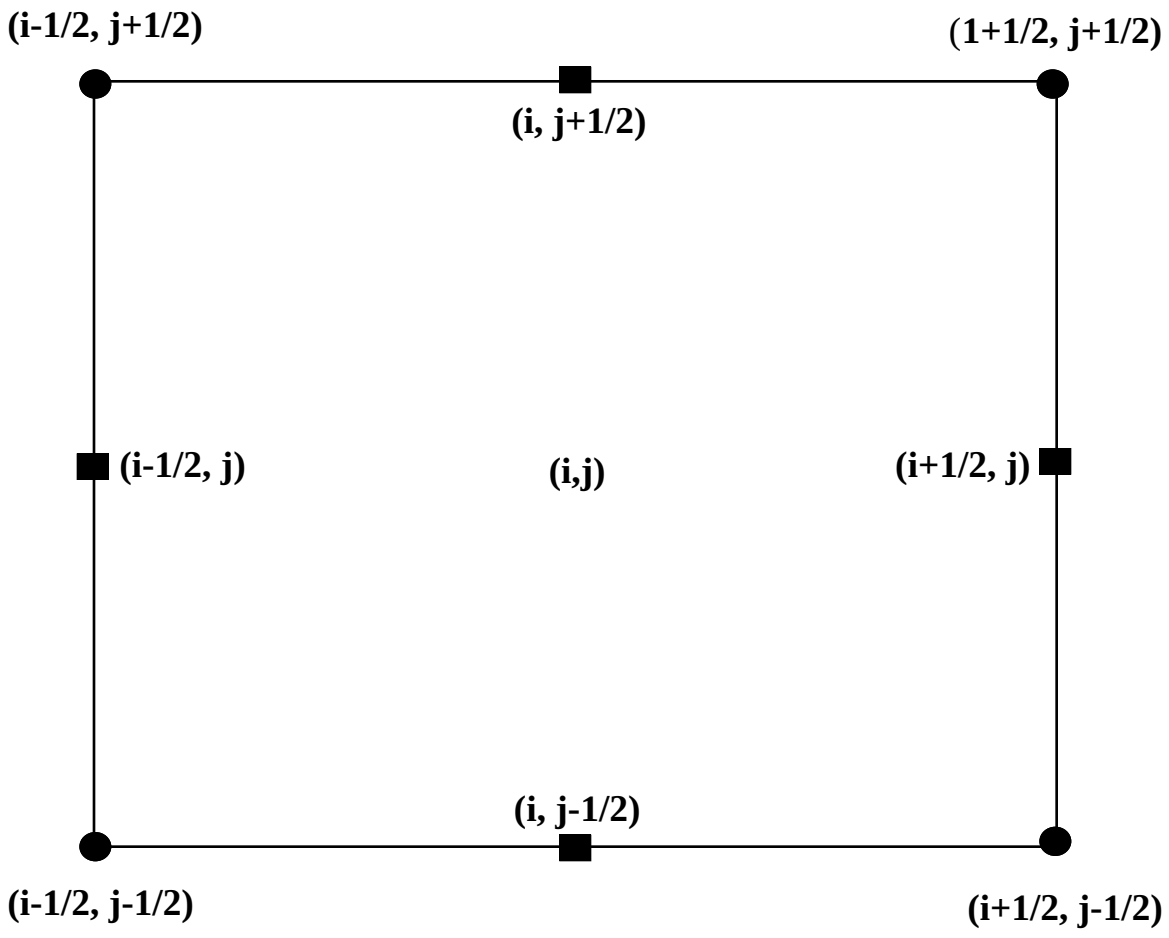

Figure 2: JCP: Morel, Roberts, and Shashkov, "A Local Support-Operator Diffusion Discretization Scheme for Quadrilateral r-z Meshes."

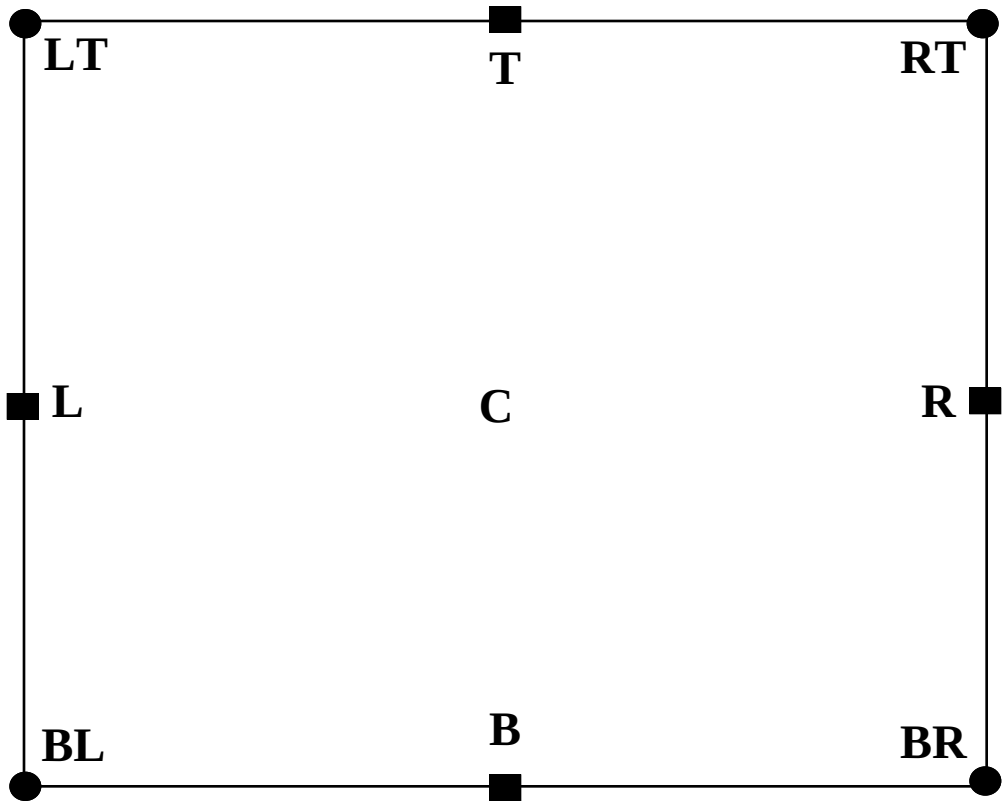

Figure 3: JCP: Morel, Roberts, and Shashkov, "A Local Support-Operator Diffusion Discretization Scheme for Quadrilateral r-z Meshes."

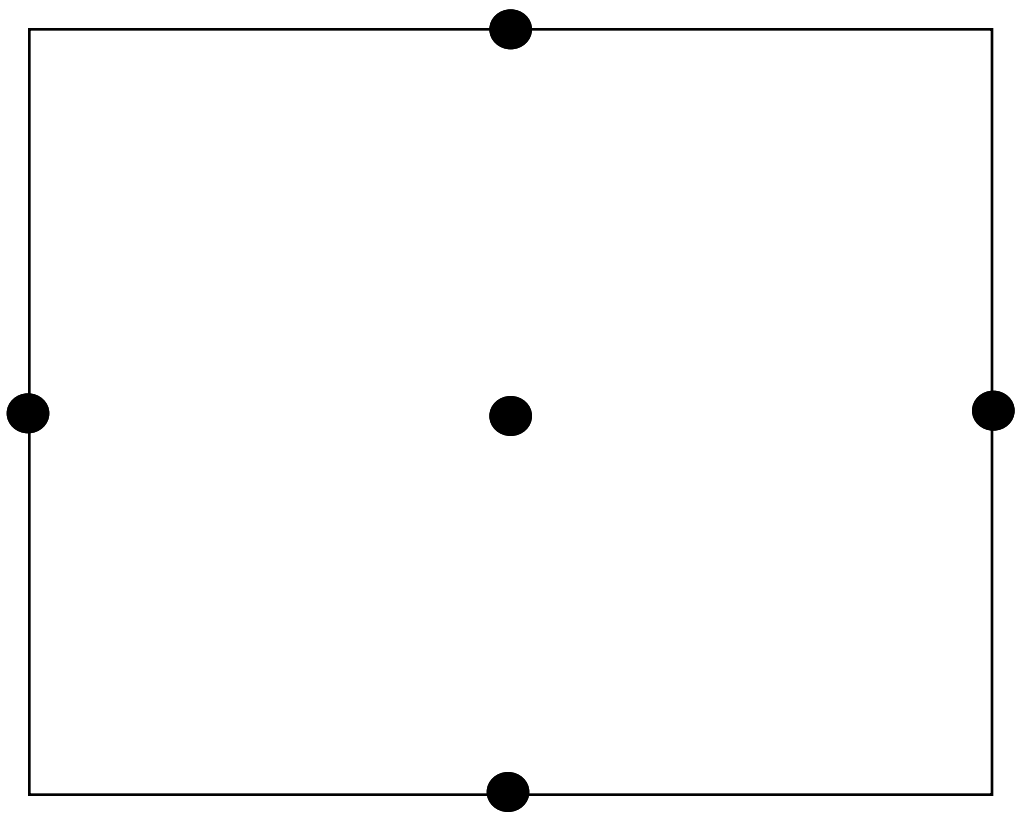

Figure 4: JCP: Morel, Roberts, and Shashkov, "A Local Support-Operator Diffusion Discretization Scheme for Quadrilateral r-z Meshes."

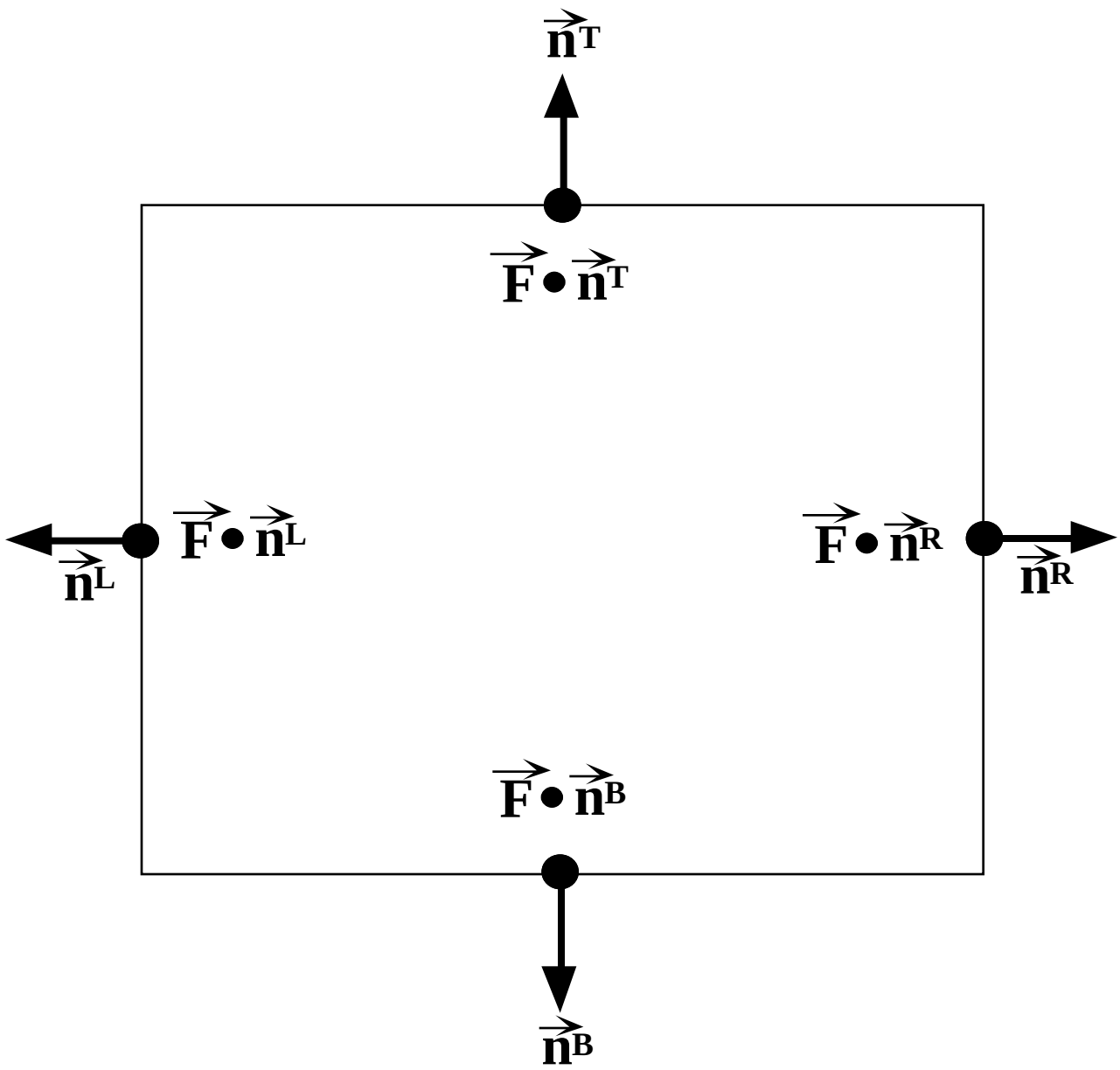

Figure 5: JCP: Morel, Roberts, and Shashkov, "A Local Support-Operator Diffusion Discretization Scheme for Quadrilateral r-z Meshes."

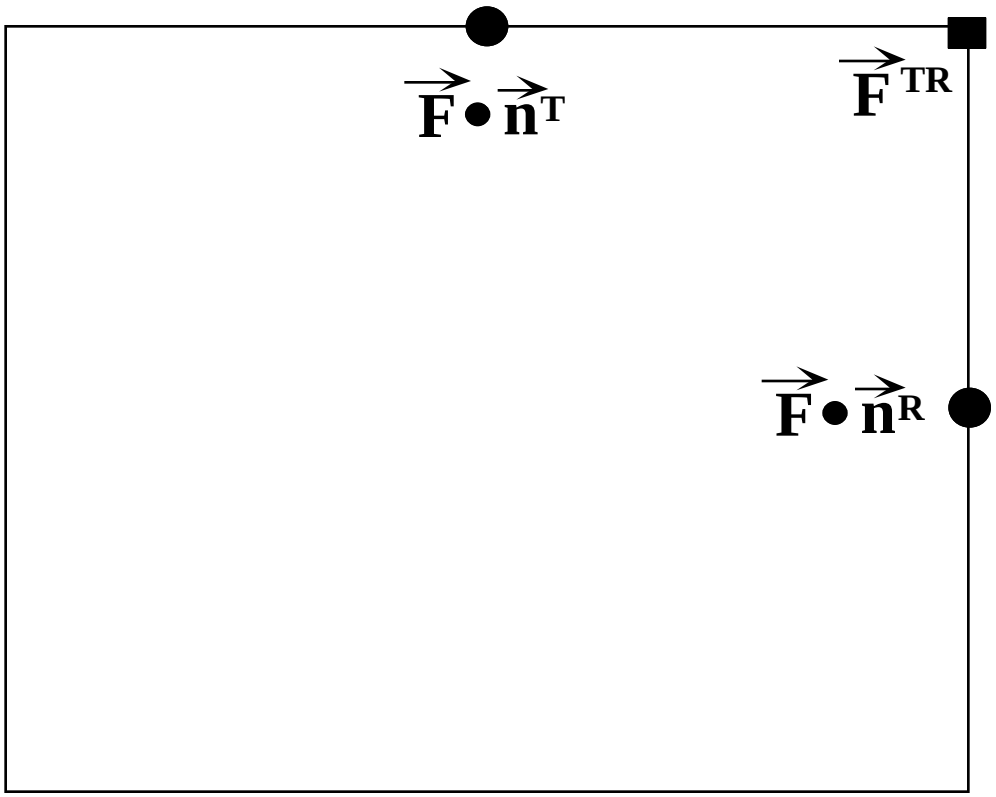

Figure 6: JCP: Morel, Roberts, and Shashkov, "A Local Support-Operator Diffusion Discretization Scheme for Quadrilateral r-z Meshes."

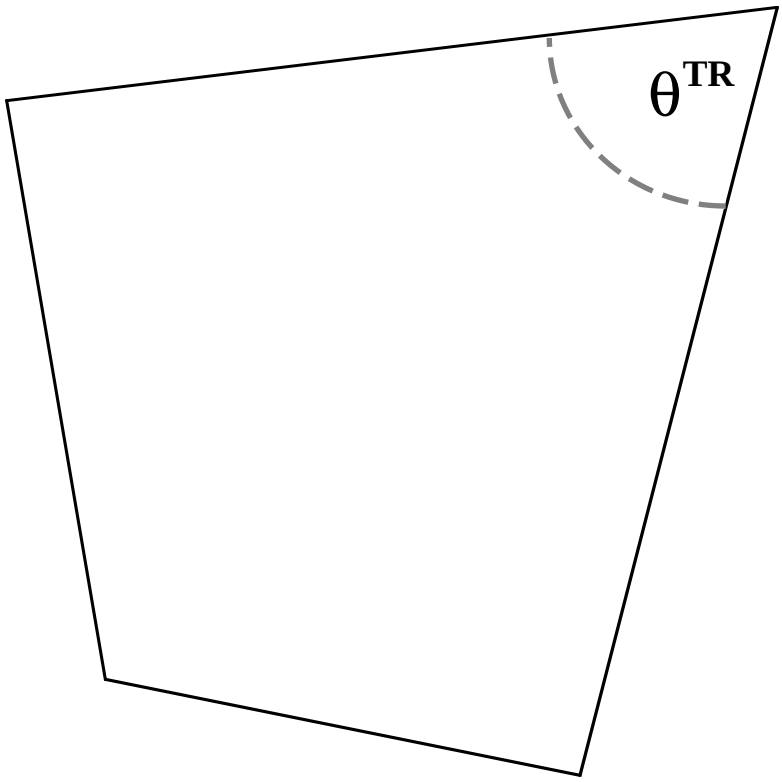

Figure 7: JCP: Morel, Roberts, and Shashkov, "A Local Support-Operator Diffusion Discretization Scheme for Quadrilateral r-z Meshes."

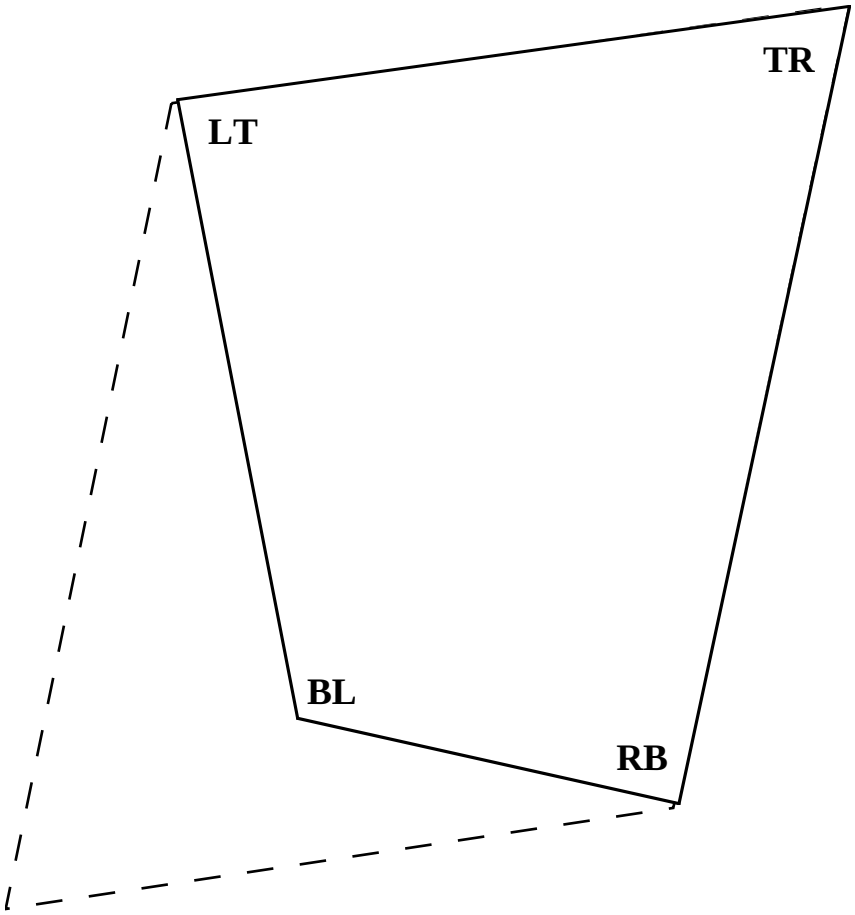

Figure 8: JCP: Morel, Roberts, and Shashkov, "A Local Support-Operator Diffusion Discretization Scheme for Quadrilateral r-z Meshes."

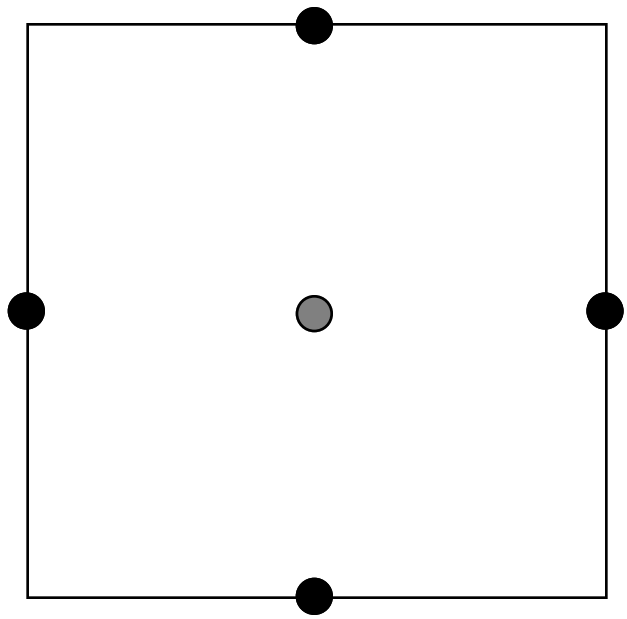

Figure 9: JCP: Morel, Roberts, and Shashkov, "A Local Support-Operator Diffusion Discretization Scheme for Quadrilateral r-z Meshes."

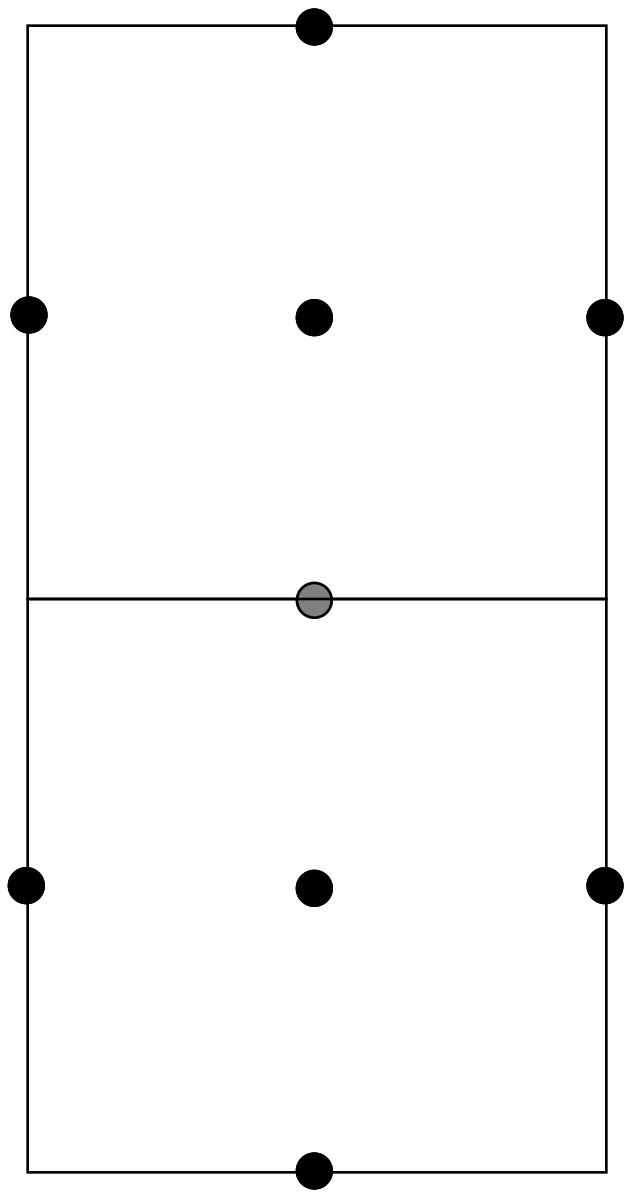

Figure 10: JCP: Morel, Roberts, and Shashkov, "A Local Support-Operator Diffusion Discretization Scheme for Quadrilateral r-z Meshes."

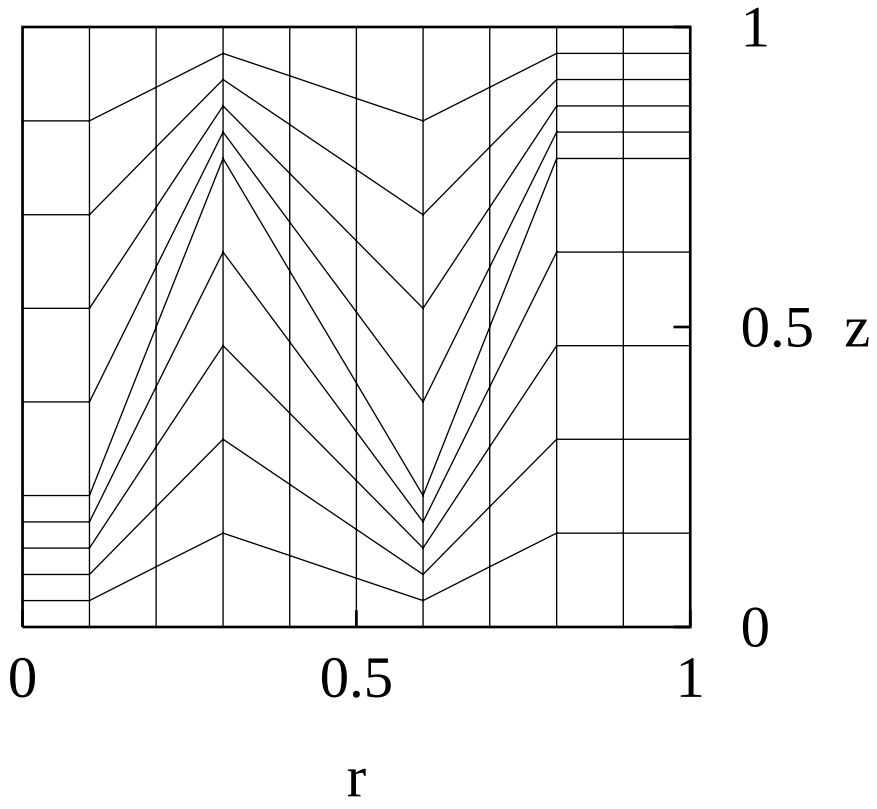

Figure 11: JCP: Morel, Roberts, and Shashkov, "A Local Support-Operator Diffusion Discretization Scheme for Quadrilateral r-z Meshes."

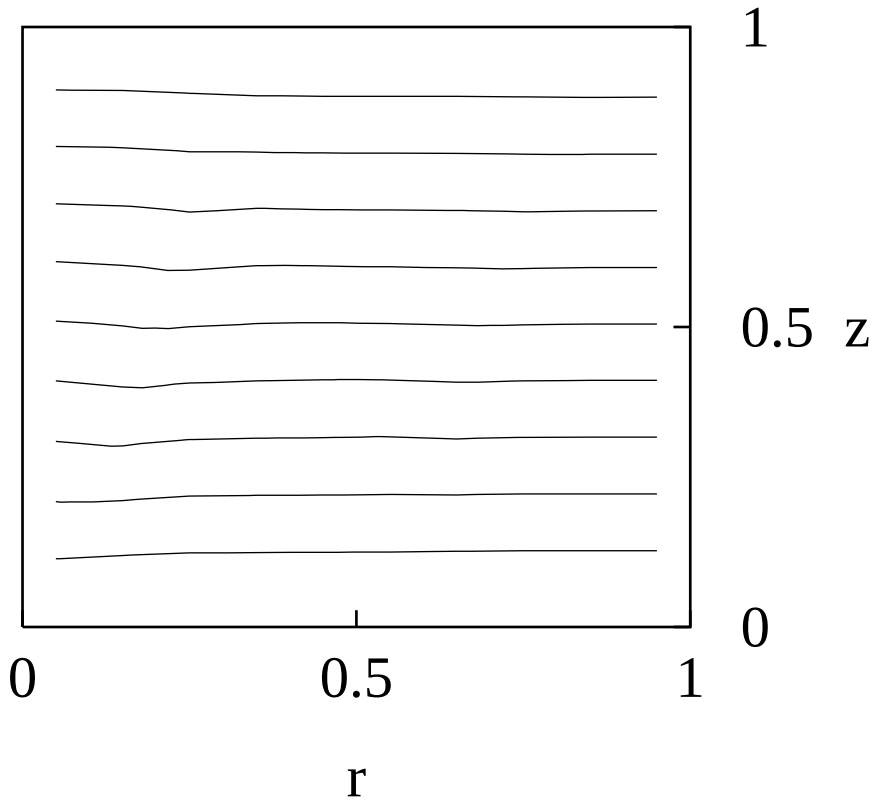

Figure 12: JCP: Morel, Roberts, and Shashkov, "A Local Support-Operator Diffusion Discretization Scheme for Quadrilateral r-z Meshes."

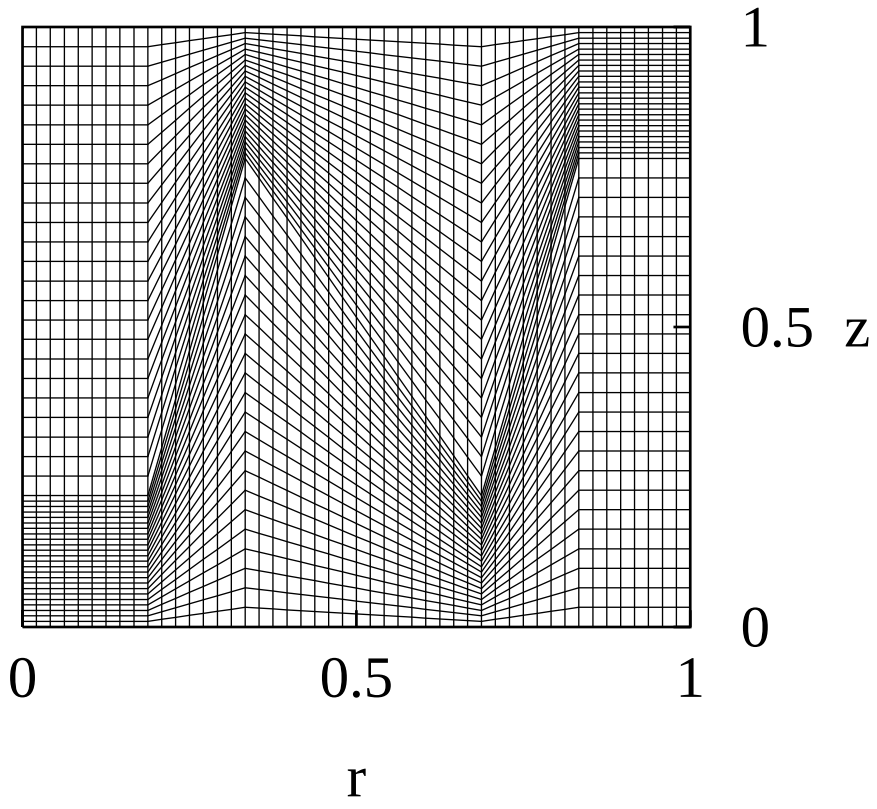

Figure 13: JCP: Morel, Roberts, and Shashkov, "A Local Support-Operator Diffusion Discretization Scheme for Quadrilateral r-z Meshes."

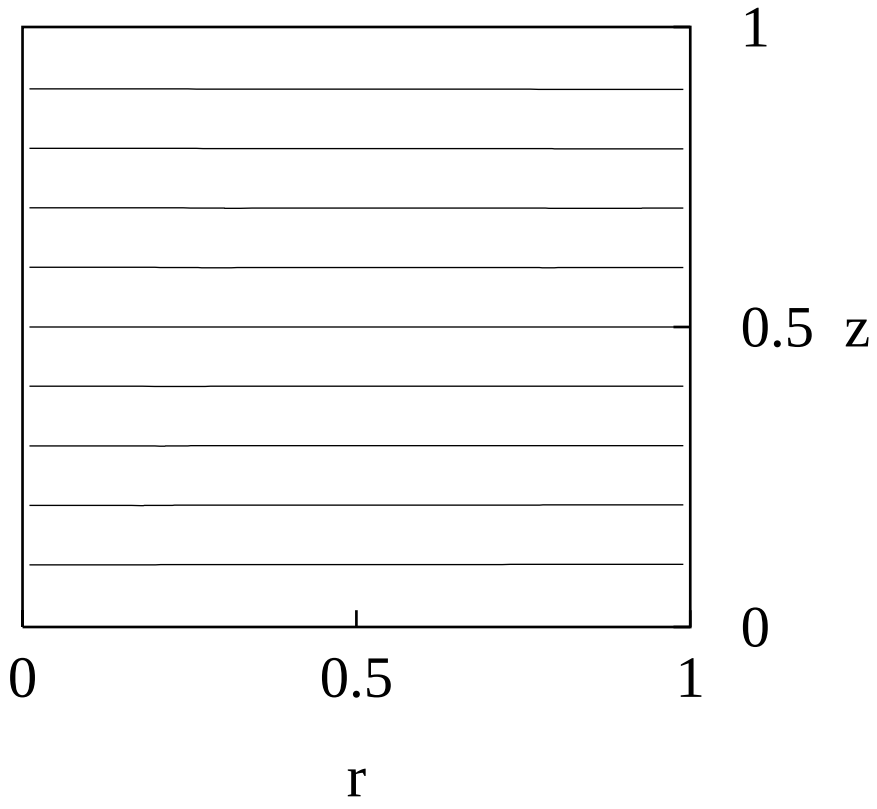

Figure 14: JCP: Morel, Roberts, and Shashkov, "A Local Support-Operator Diffusion Discretization Scheme for Quadrilateral r-z Meshes."

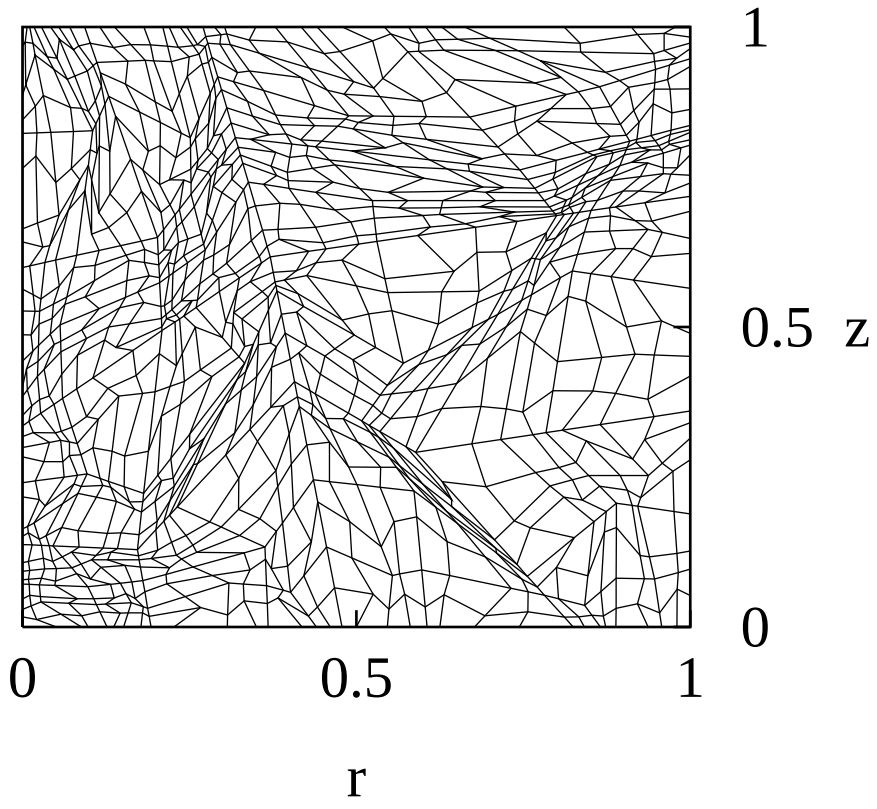

Figure 15: JCP: Morel, Roberts, and Shashkov, "A Local Support-Operator Diffusion Discretization Scheme for Quadrilateral r-z Meshes."

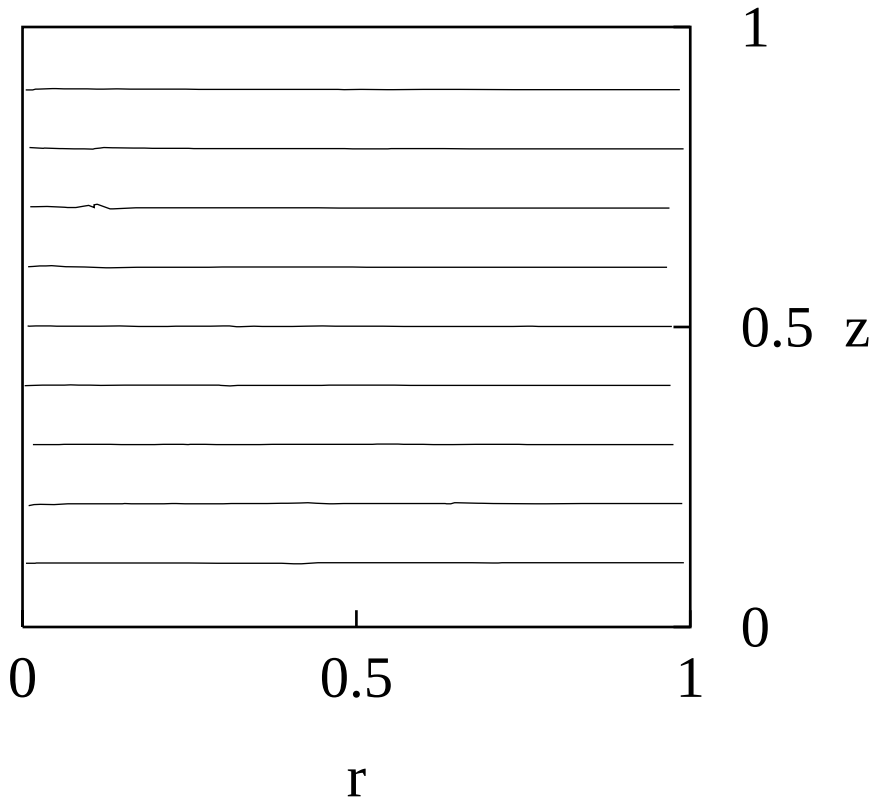

Figure 16: JCP: Morel, Roberts, and Shashkov, "A Local Support-Operator Diffusion Discretization Scheme for Quadrilateral r-z Meshes."

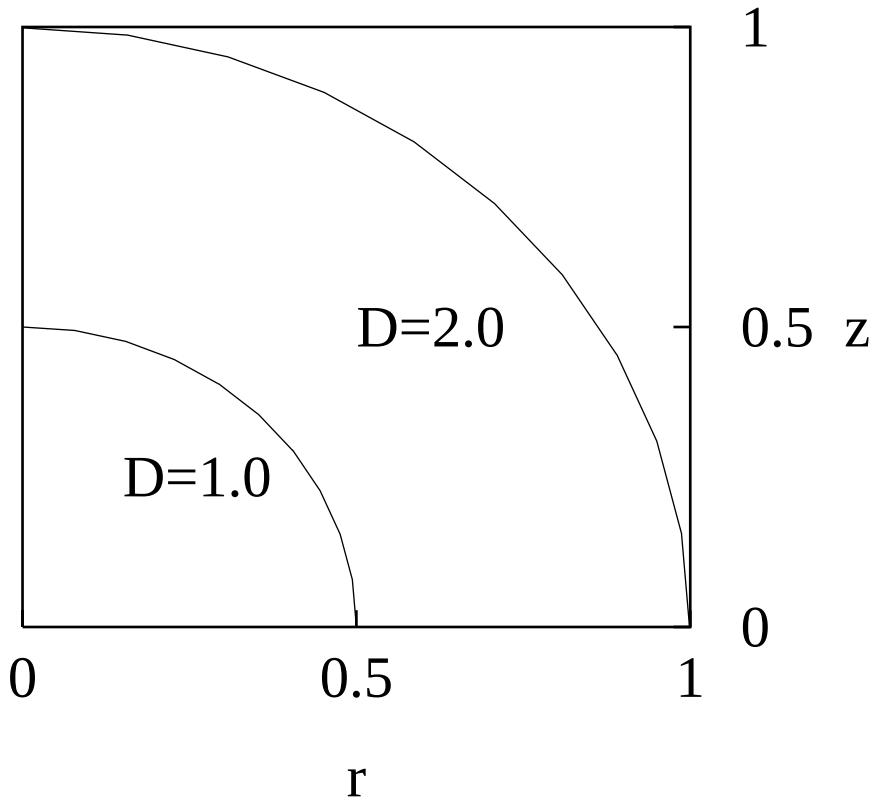

Figure 17: JCP: Morel, Roberts, and Shashkov, "A Local Support-Operator Diffusion Discretization Scheme for Quadrilateral r-z Meshes."

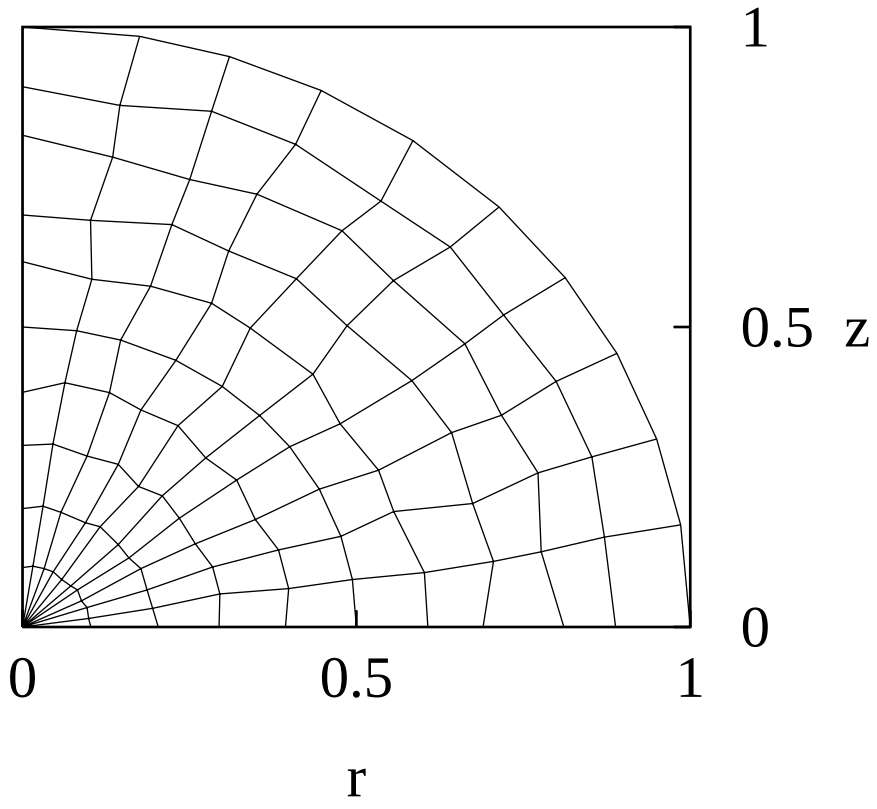

Figure 18: JCP: Morel, Roberts, and Shashkov, "A Local Support-Operator Diffusion Discretization Scheme for Quadrilateral r-z Meshes."

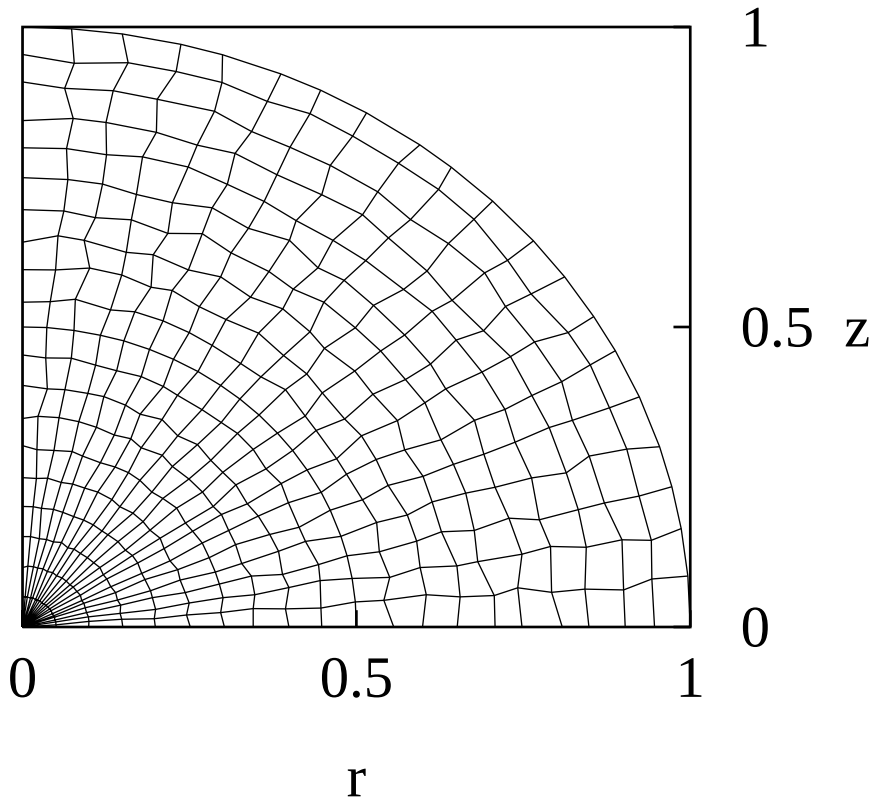

Figure 19: JCP: Morel, Roberts, and Shashkov, "A Local Support-Operator Diffusion Discretization Scheme for Quadrilateral r-z Meshes."

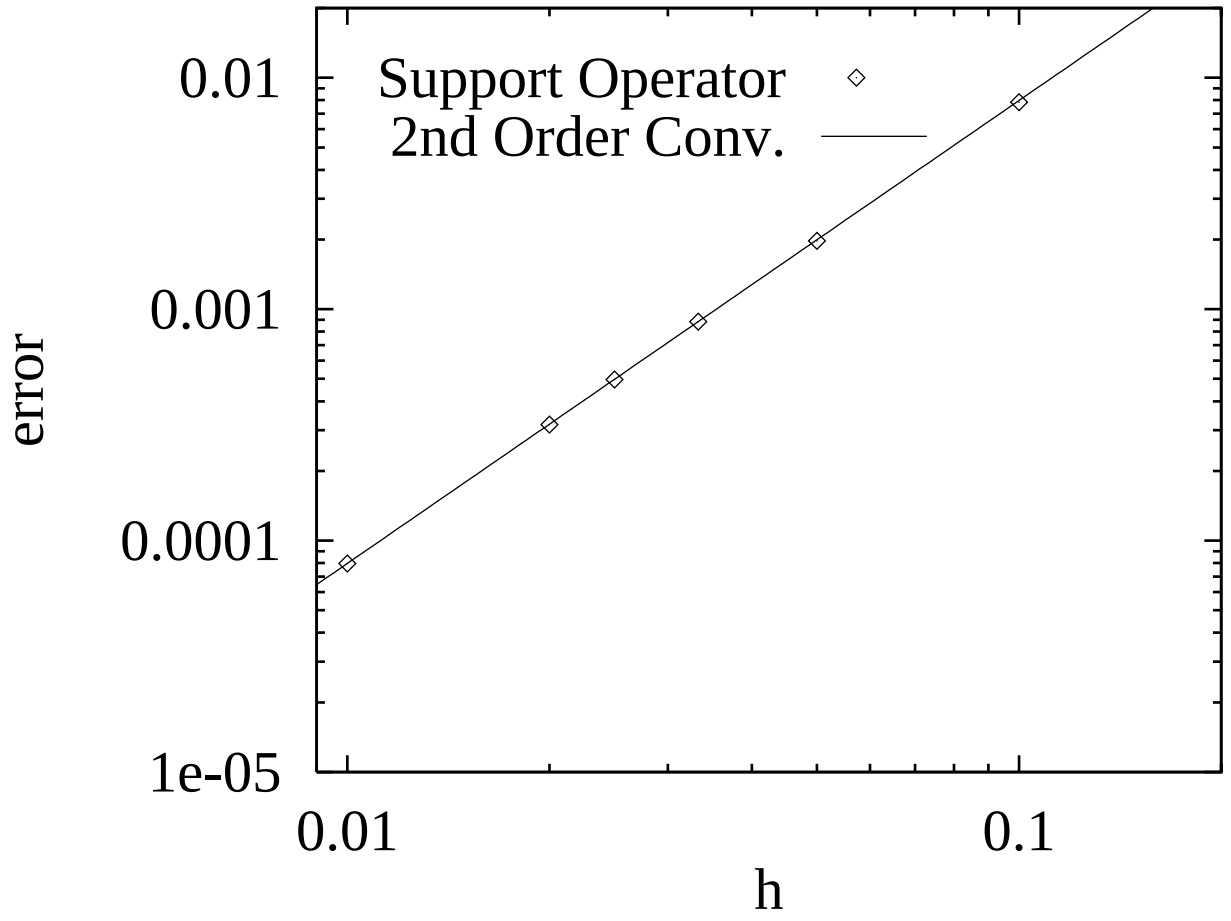
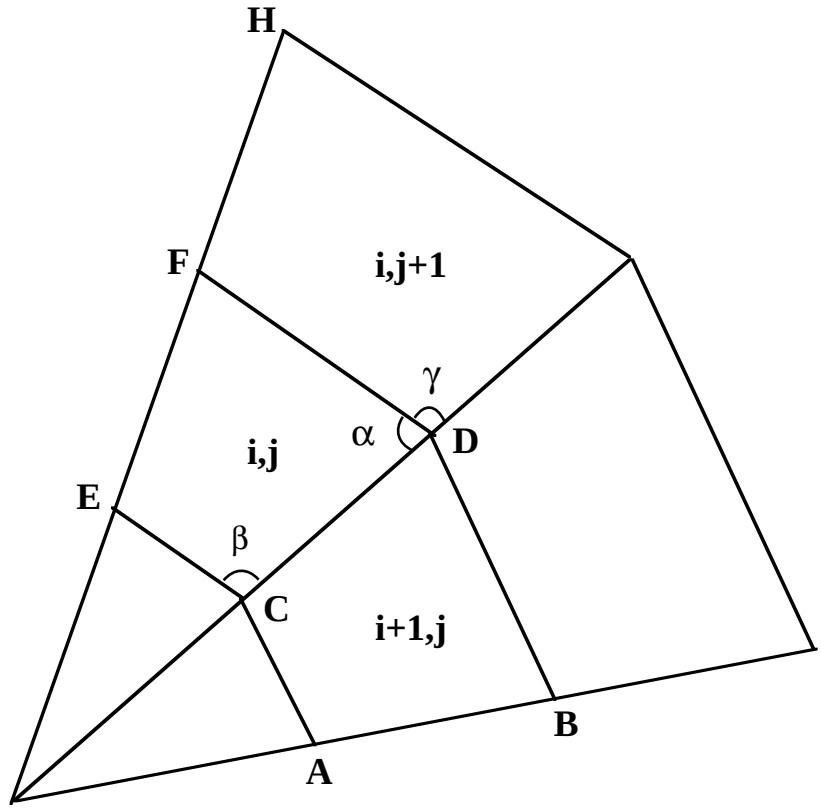
Figure 20: JCP: Morel, Roberts, and Shashkov, "A Local Support-Operator Diffusion Discretization Scheme for Quadrilateral r-z Meshes."